Nonhomogeneous volume conduction effects affecting needle electromyography: an analytical and simulation study

Xuesong Luo[1,3], Shaoping Wang[1], Seward B. Rutkove[2] and Benjamin Sanchez[3] ‡

[1]Department of Automation Science and Electric Engineering, Beijing Advanced Innovation Center for Big Data-Based Precision Medicine, Beihang University, Beijing 100083, China.
[2]Department of Neurology, Beth Israel Deaconess Medical Center, Harvard Medical School, Boston, MA 02215, USA.
[3]Sanchez Research Lab, Department of Electrical and Computer Engineering, University of Utah, Salt Lake City, UT 84112-9206, USA.

E-mail: benjamin.sanchez@utah.edu

Abstract. *Objective*: Needle electromyography (EMG) is used to study the electrical behavior of myofiber properties in patients with neuromuscular disorders. However, due to the complexity of electrical potential spatial propagation in nonhomogeneous diseased muscle, a comprehensive understanding of volume conduction effects remains elusive. Here, we develop a framework to study the conduction effect of extracellular abnormalities and electrode positioning on extracellular local field potential (LFP) recordings. *Methods*: The framework describes the macroscopic conduction of electrical potential in an isotropic, nonhomogeneous (i.e., two tissue) model. Numerical and finite element model simulations are provided to study the conduction effect in prototypical monopolar EMG measurements. *Results*: LFPs recorded are influenced in amplitude, phase and duration by the electrode position in regards to the vicinity of tissue with different electrical properties. *Conclusion*: The framework reveals the influence of multiple mechanisms affecting LFPs including changes in the distance between the source – electrode and tissue electrical properties. *Clinical significance*: Our modeled predictions may lead to new ways for interpreting volume conduction effects on recorded EMG activity, for example in neuromuscular diseases that cause structural and compositional changes in muscle tissue. These change will manifest itself by changing the electric properties of the conductor media and will impact recorded potentials in the area of affected tissue.

Keywords: Needle electromyography, neuromuscular disorders, local field potential, skeletal muscle.

‡ Corresponding author: Dr. Benjamin Sanchez, Sorenson Molecular Biotechnology Building, Office 3721, 36 South Wasatch Drive, University of Utah, Salt Lake City, UT 84112-9206, USA, phone: (801) 585-9535, email: benjamin.sanchez@utah.edu.

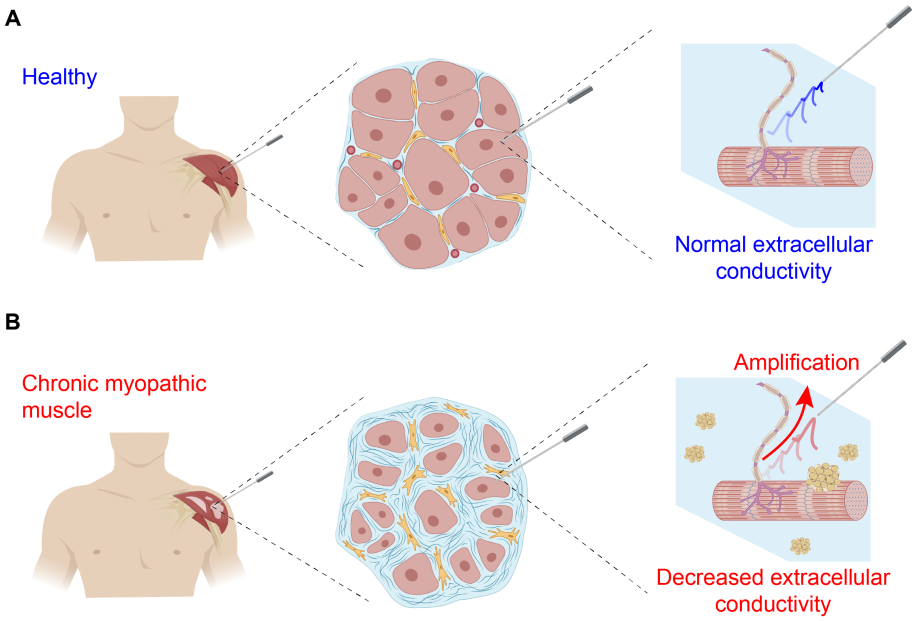

Figure 1. Illustration of extracellular local field potentials (LFPs) spatial propagation in needle electromyography towards a distant recording needle electrode. The LFPs are filtered (attenuated or amplified) by the frequency characteristics determined by the electrical properties (EP) of diseased muscle extracellular environment. In the figure, decreased conductivity illustrated by pockets of fat infiltration as seen in chronic myopathic disease increase the amplitude of LFPs (Fukada et al. 2010).

1. Introduction

Needle electromyography (EMG) remains the standard "go-to" test used to evaluate neuromuscular disorders in adult population (Katirji 2014). In standard EMG (Figure 1 A), a monopolar (1-electrode) or concentric (2-electrode) needle is inserted through the skin and subcutaneous fat into a muscle of interest using anatomical landmarks. Once placed in the muscle, it is gently maneuvered through the tissue to intentionally irritate and injure individual myocyte membranes with the limb at rest. With each passage of the needle, electrical discharges are observed from the resulting membrane depolarization. Through pattern recognition, the examiner seeks to identify abnormal spontaneous electrical potentials, including repetitive discharges from single muscle fibers (e.g., fibrillation potentials and myotonic potentials) or from groups of muscle fibers (e.g., fasciculation potentials and myokymic potentials). Once this part of the procedure is completed, the patient is then asked to contract the muscle and the characteristics of the voluntary motor unit potentials are evaluated as well as the recruitment patterns.

EMG records low frequency extracellular local field potentials (LFPs) generated by "electrically-active" motor units. In nonhomogeneous diseased muscle as shown in Figure 1, the filtering characteristics of the tissue affecting the morphology (i.e., in amplitude, latency and phase) of LFPs are likely determined by structural (e.g., myofiber

atrophy or tissue necrosis) and compositional (e.g., fatty infiltration or interstitial edema) alterations affecting the extracellular conducting medium (Nagy et al. 2019). These tissue alterations are a main determinant of the frequency-filtering properties of LFPs and their effect on far-distant surface EMG recordings has been exhaustively studied in (Mesin & Farina 2004, Mesin 2013*a*, Mesin 2013*b*). Here, we expand these studies and develop simplified analytical models to describe electrical potentials recorded in nonhomogeneous muscle during a needle EMG test, i.e., the clinical approach to diagnose neuromuscular disorders (de Morentin et al. 2021).

Experimental observation of volume conduction and its relevance to features on needle EMG has been studied for decades. Work going back to the 1980s assessed the impact of depolarizing neurons or myofibers through a volume conductor. For example, studies have assessed how the distance between the source of the potential and recording electrodes will impact the observed responses and were especially important in the field of evoked potentials (Machida et al. 1983, Yamada et al. 1982). Dimitru also investigated the effects of the position of the recording electrodes to the potential source in a review paper in 1991 that summarized beautifully our understanding of potentials that stands to this day (Dumitru & Delisa 1991). These studies showed how the amplitude and morphology of common waveforms, including fibrillation and motor unit potentials, would change depending on the distance between the recording electrode and source. However, there was always an assumption of homogeneous, conductive media. In most neurological disorders, in contrast, this is known not to be the case. In disorders with inflammation, the presence of edema could actually increase tissue conductivity with the muscle (Sanchez & Rutkove 2017). Conversely, in conditions in which there is substantial fat deposition, such as in a muscular dystrophy or chronic neurogenic disease, the overall conductivity may decrease. Although some have studied the impact of subcutaneous fat on surface EMG measurements (Lowery et al. 2002, Blok et al. 2002, Lowery et al. 2004), to our knowledge, none have sought to assess the impact of such additional components in a nonhomogeneous pattern within the muscle itself.

This work aims to contribute to the understanding macroscopic nonhomogeneous volume conduction effects on monopolar needle EMG. For this, we develop a theoretical framework to model electrical potential recordings in a nonhomogeneous volume conductor composed of two separate, interspersed and both tissues with different electrical properties. The framework is general enough to describe an arbitrary boundary between the tissues with the voltage recording electrode in a different tissue from the (current) source or even at the boundary between tissues. We develop in Section 2 and 3 a framework to model quasi-stationary and transient LFPs, respectively. Two simplified case studies are analyzed in Section 4 considering the effect of subcutaneous fat and muscle fat deposition in Section 5. Section 6 compares our theoretical prediction against FEM simulations, which confirm the usefulness of the novel framework presented. Finally, the main findings are discussed in Section 7.

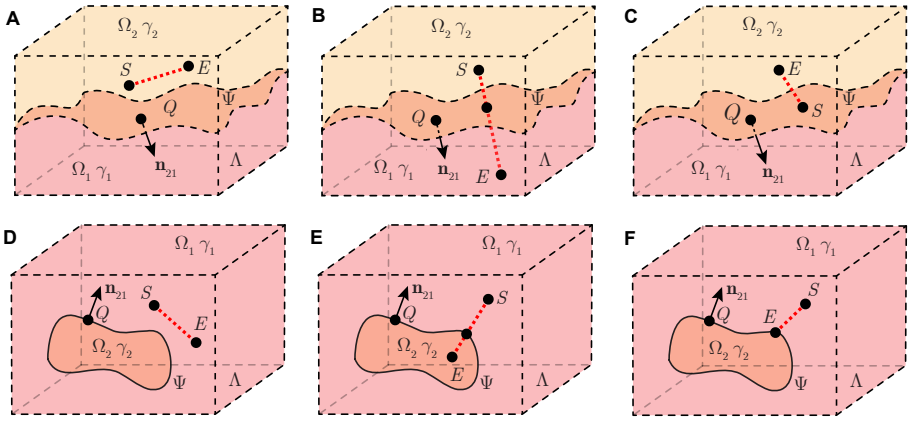

Figure 2. Schematic illustrating a nonhomogeneous tissue containing two sub-domains Ω_1 and Ω_2 in full space Λ with isotropic admittivity γ_1 and γ_2, respectively. Domain Ω_2 is a infinite open region (A, B, C) or limited closed region (D, E, F). In this model, the point Q with coordinates $\mathbf{r}_\mathrm{Q} := (x_\mathrm{Q}, y_\mathrm{Q}, z_\mathrm{Q})$ is on Ψ, the latter the surface which defines the boundary between Ω_1 and Ω_2. Vector $\mathbf{n}_{21}$ is a normal vector of Ψ at $\mathbf{r}_\mathrm{Q}$, which is pointing from Ω_2 to Ω_1. A current source S at $\mathbf{r}_\mathrm{S} := (x_\mathrm{S}, y_\mathrm{S}, z_\mathrm{S})$ generates current in the model. Electrode E at $\mathbf{r}_\mathrm{E} := (x_\mathrm{E}, y_\mathrm{E}, z_\mathrm{E})$ records the resultant electrical potential. The current source S and voltage measuring electrode E are placed in the same domain (A, D) or in different domains (B, E). In addition, either of S and E can be on the boundary Ψ (C, F).

2. Quasi-stationary volume conduction framework in a nonhomogeneous domain

We consider a nonhomogeneous tissue $\Lambda := \Omega_1 \bigcup \Omega_2 = \mathbb{R}^3$ containing two arbitary domains Ω_1, Ω_2 and their boundary $\Psi := \Omega_1 \cap \Omega_2$ in full space. The boundary can be either an inifnite surface (Figure 2 A, B, C) or a limited closed surface (Figure 2 D, E, F). The system of coordinates $\mathbf{r} := (x, y, z) \in \Lambda$ defines the position of the current source and voltage measuring electrodes S at $\mathbf{r}_\mathrm{S} := (x_\mathrm{S}, y_\mathrm{S}, z_\mathrm{S})$ and E at $\mathbf{r}_\mathrm{E} := (x_\mathrm{E}, y_\mathrm{E}, z_\mathrm{E})$, respectively, with $\mathbf{r}_\mathrm{S} \neq \mathbf{r}_\mathrm{E}$. Electrode S, E are capable to locate in the same domain (Figure 2 A, D) and in different domains (Figure 2 B, E). In addition, either of S, E can be placed on the boundary (Figure 2 C, F). To develop a biophysic-driven model for aforementioned nonhomogeneous tissue, we make the following assumptions: (1), the source and voltage recording electrodes are dimensionless; (2), each sub-domain has isotropic, frequency-dependent electrical properties; and (3), there are no free charges in the model.

2.1. Governing equation

In order to build an analytical model describing the spatial propagation of electrical potential through skeletal muscle tissue as a volume conductor requires to define the genesis of electrical current, either endogenously (e.g., action current) or exogenously (e.g., externally induced electrical current), generated within the model. Firstly we

consider a sinusoidal electrical current $i(t) := I\cos(\omega_k t)$ generated by the current source S positioned at $\mathbf{r}_{\mathrm{S}}$ with current sink at infinity, where $t \in \mathbb{R}$ (s) is the time variable, $I \in \mathbb{R}$ (A) is the current amplitude at the measurement frequency $\omega_k \in \mathbb{R}$ (rad s^{-1}). An electrode E is placed at $\mathbf{r}_{\mathrm{E}}$ to determine the electrical potential with reference zero potential at infinity (in practice, this is the ground electrode in EMG measurements). Since the electrical potential generated by sink infinitely far away, it has no impact on the region of source S that we are interested to study. Thus the electrical potential recorded by E is stimulated by source S only. The admittivity $\gamma \in \mathbb{C}$ (S m^{-1}) in Λ expressed explicitly as a function of the position and measurement frequency is

$$\gamma(\mathbf{r},\omega_k) := \begin{cases} \gamma_i(\omega_k) & \text{if } \mathbf{r} \text{ in } \Omega_i \\ (\gamma_1(\omega_k)+\gamma_2(\omega_k))/2 & \text{if } \mathbf{r} \text{ on } \Psi, \end{cases} \tag{1}$$

where $i \in \{1,2\}$ is the domain index, $\gamma_{\{1,2\}}(\omega_k) := \sigma_{\{1,2\}}(\omega_k) + j\omega_k\varepsilon_{\{1,2\}}(\omega_k)$, $\sigma_{\{1,2\}}(\omega_k) \in \mathbb{R}_{>0}$ (S m^{-1}) and $\varepsilon_{\{1,2\}}(\omega_k) \in \mathbb{R}_{>0}$ (F m^{-1}) are the isotropic conductivity and permittivity, i.e., γ_1 in Ω_1 and γ_2 in Ω_2, respectively, and $j = \sqrt{-1}$ is the imaginary unit (dimensionless).

From Maxwell equations in quasi-stationary regime (Maxwell 1873), the generalized Poisson equation with respect to the electrical potential distribution $U(\mathbf{r},\omega_k) \in \mathbb{C}$ (V) generated by the current source S applying current I is

$$\nabla\cdot[\gamma(\mathbf{r},\omega_k)\nabla U(\mathbf{r},\omega_k)] = -I\delta(\mathbf{r}-\mathbf{r}_{\mathrm{S}}), \tag{2}$$

in which ∇ is the vector differential operator, and $\delta(\mathbf{r})$ is the Dirac delta function. Henceforth, we omit both the spatial and the frequency dependence of both the admittivity $\gamma(\mathbf{r},\omega_k)$ and potential $U(\mathbf{r},\omega_k)$ as γ and U, respectively, for the sake of notation clarity.

Next, we define an arbitrary point Q with coordinates $\mathbf{r}_{\mathrm{Q}} := (x_{\mathrm{Q}}, y_{\mathrm{Q}}, z_{\mathrm{Q}})$ on boundary Ψ. Vector $\mathbf{n}_{21}(\mathbf{r}_{\mathrm{Q}})$ is a normal vector of surface Ψ at $\mathbf{r}_{\mathrm{Q}}$ pointing from Ω_2 to Ω_1 and $\hat{\mathbf{n}}_{21}(\mathbf{r}_{\mathrm{Q}})$ is its unit vector, i.e., $\hat{\mathbf{n}}_{21}(\mathbf{r}_{\mathrm{Q}}) := \mathbf{n}_{21}(\mathbf{r}_{\mathrm{Q}}) / |\mathbf{n}_{21}(\mathbf{r}_{\mathrm{Q}})|$, where $|\cdot|$ is the L_2 norm. According to (1) and considering that the gradient of admittivity is $\nabla\gamma = (\gamma_1-\gamma_2)\,\delta(\mathbf{r}-\mathbf{r}_{\mathrm{Q}})\,\hat{\mathbf{n}}_{21}(\mathbf{r}_{\mathrm{Q}})$, (2) gives

$$\nabla^2 U = -\frac{I\delta(\mathbf{r}-\mathbf{r}_{\mathrm{S}})}{\gamma} - 2\Gamma\delta(\mathbf{r}-\mathbf{r}_{\mathrm{Q}})\frac{\partial U}{\partial \mathbf{n}_{21}(\mathbf{r}_{\mathrm{Q}})}\cdot\mathbf{n}_{21}(\mathbf{r}_{\mathrm{Q}}), \tag{3}$$

where $\mathbf{r} \neq \mathbf{r}_{\mathrm{S}}$ and $\Gamma \in \mathbb{C}$ is the reflection coefficient (dimensionless) on Ψ between Ω_1 and Ω_2 defined as $\Gamma := (\gamma_1-\gamma_2)/(\gamma_1+\gamma_2)$. Finally, (3) determines the electrical potential distribution U in Λ generated by unique current source S at an arbitrary position $\mathbf{r}_{\mathrm{S}}$.

2.2. Electrical potential distribution

To solve (3), we define an integral transformation operator $\mathcal{G}_\Psi[\cdot]$ here with respect to arbitrary surface Ψ as

$$f(\mathbf{r}) \mapsto \mathcal{G}_\Psi[f(\mathbf{r})] := \frac{1}{2\pi}\iint_\Psi \frac{\partial f(\mathbf{r}_{\mathrm{Q}})}{\partial \mathbf{n}_{21}(\mathbf{r}_{\mathrm{Q}})}\cdot\frac{\mathbf{n}_{21}(\mathbf{r}_{\mathrm{Q}})\,\mathrm{d}\Psi(\mathbf{r}_{\mathrm{Q}})}{|\mathbf{r}-\mathbf{r}_{\mathrm{Q}}|},$$

where $f(\mathbf{r}) \in \mathbb{R}$ is an arbitrary function defined in $\mathbb{R}^3$, and $\mathrm{d}\Psi\left(\mathbf{r}_{\mathrm{Q}}\right)$ represents the area of the micro-elements $\mathrm{d}\Psi$ on surface Ψ at position $\mathbf{r}_{\mathrm{Q}}$. Based on $\mathcal{G}_{\Psi}\left[\cdot\right]$, we can also define a m^{th}-order iterative transform $\mathcal{G}_{\Psi}^{m}\left[\cdot\right]$ as

$$f\left(\mathbf{r}\right) \mapsto \mathcal{G}_{\Psi}^{m}\left[f\left(\mathbf{r}\right)\right] := \overbrace{\mathcal{G}_{\Psi}\left[\mathcal{G}_{\Psi}\left[\,\cdots \mathcal{G}_{\Psi}\right.\right.}^{m}\left.\left.\left[f\left(\mathbf{r}\right)\right]\cdots\right]\right],$$

where $m \in \mathbb{N}_0$. Then, applying the method of Green's function (Cohl & Tohline 1999) to (3) gives an integral equation for the electrical potential, namely

$$U = \frac{I}{4\pi\gamma_{\mathrm{S}}\left|\mathbf{r}-\mathbf{r}_{\mathrm{S}}\right|} + \Gamma\mathcal{G}_{\Psi}\left[U\right], \tag{4}$$

where $\gamma_{\mathrm{S}} := \gamma\left(\mathbf{r}_{\mathrm{S}}\right)$ refers to the admittivity at position $\mathbf{r}_{\mathrm{S}}$. Using variational iteration method (He 1999, Wazwaz 2007) to solve (4), we define the approximated electrical potential $\widetilde{U}^{(p)}$ as

$$\widetilde{U}^{(p)} := \begin{cases} \frac{I}{4\pi\gamma_{\mathrm{S}}\left|\mathbf{r}-\mathbf{r}_{\mathrm{S}}\right|} & \text{if } p = 0 \\ \frac{I}{4\pi\gamma_{\mathrm{S}}\left|\mathbf{r}-\mathbf{r}_{\mathrm{S}}\right|} + \Gamma\mathcal{G}_{\Psi}\left[\widetilde{U}^{(p-1)}\right] & \text{else} \end{cases} \tag{5}$$

where $p \in \mathbb{N}_0$ is the order of the approximation. Then U can be approximated as $U = \lim_{p\to\infty}\widetilde{U}^{(p)}$. Since $|\Gamma| < 1$, we can apply operator $\mathcal{G}_{\Psi}^{m}\left[\cdot\right]$ to simplify (5) as

$$\widetilde{U}^{(p)} = \frac{I}{4\pi\gamma_{\mathrm{S}}}\sum_{m=0}^{p}\Gamma^{m}K_{\Psi}^{(m)}(\mathbf{r},\mathbf{r}_{\mathrm{S}}), \tag{6}$$

where

$$K_{\Psi}^{(m)}(\mathbf{r},\mathbf{r}_{\mathrm{S}}) := \mathcal{G}_{\Psi}^{m}\left[\frac{1}{\left|\mathbf{r}-\mathbf{r}_{\mathrm{S}}\right|}\right] \tag{7}$$

is a m^{th}-order geometrical constant (m^{-1}) determined by the shape of surface Ψ and the relative position between the source $\mathbf{r}_{\mathrm{S}}$ and the potential evaluating point $\mathbf{r}$ with respect to Ψ. Then, the 1^{st}-order $p = 1$ approximated electrical potential $\widetilde{U}^{(1)}(\mathbf{r}_{\mathrm{E}})$ measured by the voltage recording electrode E is

$$\widetilde{U}^{(1)}(\mathbf{r}_{\mathrm{E}}) = \frac{I}{4\pi\gamma_{\mathrm{S}}}\left(\frac{1}{\left|\mathbf{r}_{\mathrm{E}}-\mathbf{r}_{\mathrm{S}}\right|} + \Gamma K_{\Psi}^{(1)}(\mathbf{r}_{\mathrm{E}},\mathbf{r}_{\mathrm{S}})\right). \tag{8}$$

3. Transient volume conduction framework in a nonhomogeneous domain

The 1^{st}-order approximated model (8) developed from (2) describes the electrical potential $\widetilde{U}^{(1)}\left(\mathbf{r}_{\mathrm{E}},\omega_k\right)$ in quasi-stationary state generated by a sinusoidal current source I at specific frequency ω_k. Using the Fourier transform method as the same rationale in (Miceli et al. 2017), it can be extended to a transient model $\widetilde{u}^{(1)}\left(\mathbf{r}_{\mathrm{E}},t\right)$ with an arbitrary waveform current source $i(t) \in \mathbb{R}$ (A) in time domain $t \in \mathbb{R}_{\geq 0}$ (s). Then, the 1^{st}-order temporal electrical potential approximation $\widetilde{u}^{(1)}\left(\mathbf{r}_{\mathrm{E}},t\right)$ recorded by voltage measuring electrode E follows from (8), namely

$$\widetilde{u}^{(1)}(\mathbf{r}_{\mathrm{E}},t) := \mathrm{Re}\left\{\mathcal{F}^{-1}\left[\frac{\mathcal{I}(\omega)}{4\pi\gamma_{\mathrm{S}}(\omega)}\left(\frac{1}{\left|\mathbf{r}_{\mathrm{E}}-\mathbf{r}_{\mathrm{S}}\right|} + \Gamma(\omega)K_{\Psi}^{(1)}(\mathbf{r}_{\mathrm{E}},\mathbf{r}_{\mathrm{S}})\right)\right]\right\}, \tag{9}$$

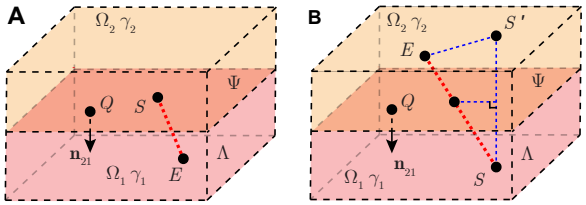

Figure 3. Case study 1 of a nonhomogeneous EMG measurement with a planar boundary in full space Λ. Plane Ψ divide full space into two half space domains Ω_1 and Ω_2 with isotropic admittivity γ_1, γ_2, respectively. Point Q with coordinates $\mathbf{r}_\mathrm{Q}$ is on Ψ. Vector $\mathbf{n}_{21}$ is a normal vector of Ψ at $\mathbf{r}_\mathrm{Q}$, which is pointing from Ω_2 to Ω_1. A point source S located at $\mathbf{r}_\mathrm{S}$ generates current in the model. Electrode E at $\mathbf{r}_\mathrm{E}$ is another point recording the electrical potential. Electrode S is available to be placed on plane Ψ (A) and inside a domain (B). Electrode E is placed at anywhere else in Λ. If $\mathbf{r}_\mathrm{S} \notin \Psi$, S' is the mirrored point of S at $\mathbf{r}_{\mathrm{S}'}$. They are mirror symmetry with respect to plane Ψ.

where $\mathcal{I}(\omega) := \mathcal{F}[i(t)] \in \mathbb{C}$ is the current spectrum of an arbitrary current signal $i(t)$; $\omega \in \mathbb{R}$ (rad s^{-1}) is the (angular) frequency variable; $\mathrm{Re}\{\cdot\}$ is the real operator; and $\mathcal{F}[\cdot]$, $\mathcal{F}^{-1}[\cdot]$ are the (inverse) Fourier transform operator.

4. Case study

4.1. Case study 1: planar boundary model

To analyze the planar boundary model, here we provide a compact analytical expression of 1$^{\mathrm{st}}$-order geometrical parameter $K_\Psi^{(1)}(\mathbf{r}_\mathrm{E}, \mathbf{r}_\mathrm{S})$ in (8) when boundary Ψ is a plane (i.e., the curvature of surface Ψ is 0). That is to consider near the recording site, subcutaneous fat tissue and underlying muscle can be seen as a plane. In this case, the source S can be placed either on the plane Ψ (Figure 3 A) or in $\Omega_{\{1,2\}}$ (Figure 3 B). The voltage recording electrode E can be positioned anywhere else in this model. According to (7) and Lemma 1 in Part A of the Supplementary Information, we have the 1$^{\mathrm{st}}$-order geometrical parameter $K_\Psi^{(1)}(\mathbf{r}_\mathrm{E}, \mathbf{r}_\mathrm{S})$ for framework $\widetilde{U}^{(1)}(\mathbf{r}_\mathrm{E})$ in case study 1 as

$$K_\Psi^{(1)}(\mathbf{r}_\mathrm{E}, \mathbf{r}_\mathrm{S}) = \begin{cases} 0 & \text{if } \mathbf{r}_\mathrm{S} \text{ on } \Psi \\ \frac{(-1)^{i-1}}{|\mathbf{r}_\mathrm{E} - \mathbf{r}_{\mathrm{S}'}|} & \text{if } \mathbf{r}_\mathrm{S} \text{ and } \mathbf{r}_\mathrm{E} \text{ in } \Omega_i \\ \frac{(-1)^{i-1}}{|\mathbf{r}_\mathrm{E} - \mathbf{r}_\mathrm{S}|} & \text{else } \mathbf{r}_\mathrm{S} \text{ in } \Omega_i \text{ and } \mathbf{r}_\mathrm{E} \text{ in } \Omega_{3-i} \text{ or on } \Psi, \end{cases} \tag{10}$$

where $i \in \{1, 2\}$, S' at $\mathbf{r}_{\mathrm{S}'}$ is the mirrored image source, i.e., $(\mathbf{r}_\mathrm{S} + \mathbf{r}_{\mathrm{S}'})/2 \in \Psi$. Substituting (10) into (8), we can find that $\mathbf{r}_\mathrm{S}$ on Ψ and when $\mathbf{r}_\mathrm{S}$ in Ω_i, $\mathbf{r}_\mathrm{E}$ in Ω_{3-i} or on Ψ share the same 1$^{\mathrm{st}}$-order electrical potential model $\widetilde{U}^{(1)}(\mathbf{r}_\mathrm{E})$, namely

$$\widetilde{U}^{(1)}(\mathbf{r}_\mathrm{E}) = \begin{cases} \frac{I}{4\pi\gamma_i}\left(\frac{1}{|\mathbf{r}_\mathrm{E} - \mathbf{r}_\mathrm{S}|} + \Gamma\frac{(-1)^{i-1}}{|\mathbf{r}_\mathrm{E} - \mathbf{r}_{\mathrm{S}'}|}\right) & \text{if } \mathbf{r}_\mathrm{S} \text{ and } \mathbf{r}_\mathrm{E} \text{ in } \Omega_i \\ \frac{I}{2\pi(\gamma_1+\gamma_2)|\mathbf{r}_\mathrm{E} - \mathbf{r}_\mathrm{S}|} & \text{else.} \end{cases} \tag{11}$$

Using (9) we can also find transient potential propagating model $\widetilde{u}^{(1)}(\mathbf{r}_\mathrm{E}, t)$.

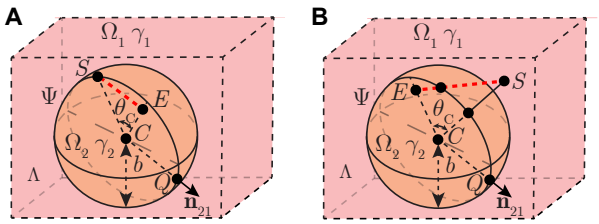

Figure 4. Case study 2 of nonhomogeneous EMG measurement with a spherical boundary in full space Λ. Spherical surface Ψ divide full space into two domains Ω_1 and Ω_2 with isotropic admittivity γ_1, γ_2, respectively. Point Q with coordinates $\mathbf{r}_Q$ is on Ψ. Vector $\mathbf{n}_{21}$ is a normal vector of Ψ at $\mathbf{r}_Q$, which is pointing from Ω_2 to Ω_1. A point source S located at $\mathbf{r}_S$ generates current in the model. Electrode E at $\mathbf{r}_E$ is another point recording the electrical potential. Electrode S is available to be placed on plane Ψ (A) and inside a domain (B). Electrode E is placed anywhere else in Λ.

4.2. Case study 2: spherical boundary model

Here we study the effect of a spherical boundary between tissues Ψ on recorded EMG. This model is an abstraction of fat deposition within the muscle as can be seen in chronic neurogenic muscle for example. In this case, the source S can be placed either on the spherical surface Ψ (Figure 4 A) or in domain $\Omega_{\{1,2\}}$ (Figure 4 B). The electrical potential recording electrode E can be placed anywhere else in Λ. Point C at $\mathbf{r}_C$ is the center of the spherical surface Ψ. According to (7) and Lemma 2 in Part B of Supplementary Information, we have the 1st-order geometrical parameter $K_\Psi^{(1)}(\mathbf{r}_E, \mathbf{r}_S)$ for framework $\widetilde{U}^{(1)}(\mathbf{r}_E)$ in case study 2 as

$$K_\Psi^{(1)}(\mathbf{r}_E, \mathbf{r}_S) = \begin{cases} \frac{b}{R_S R_E} \sum_{n=0}^{\infty} \frac{2n}{2n+1} \left(\frac{b^2}{R_S R_E}\right)^n P_n(\cos\theta_C) & \text{if} \quad R_S > b, R_E \geq b \\ \frac{1}{R_S} \sum_{n=0}^{\infty} \frac{2n}{2n+1} \left(\frac{R_E}{R_S}\right)^n P_n(\cos\theta_C) & \text{if} \quad R_S > b, R_E < b \\ -\frac{1}{R_E} \sum_{n=0}^{\infty} \frac{1}{2n+1} \left(\frac{b}{R_E}\right)^n P_n(\cos\theta_C) & \text{if} \quad R_S = b, R_E \geq b \\ -\frac{1}{b} \sum_{n=0}^{\infty} \frac{1}{2n+1} \left(\frac{R_E}{b}\right)^n P_n(\cos\theta_C) & \text{if} \quad R_S = b, R_E < b \\ -\frac{1}{R_E} \sum_{n=0}^{\infty} \frac{2n+2}{2n+1} \left(\frac{R_S}{R_E}\right)^n P_n(\cos\theta_C) & \text{if} \quad R_S < b, R_E \geq b \\ -\frac{1}{b} \sum_{n=0}^{\infty} \frac{2n+2}{2n+1} \left(\frac{R_S R_E}{b^2}\right)^n P_n(\cos\theta_C) & \text{else} \ R_S < b, R_E < b \end{cases} \tag{12}$$

where distance b is the radius of spherical surface Ψ, distance $R_S := |\mathbf{r}_S - \mathbf{r}_C|$ is the distance between the current source and center of the sphere, distance $R_E := |\mathbf{r}_E - \mathbf{r}_C|$ is the distance between voltage recording electrode and the center of the sphere, $\theta_C := \cos^{-1}\left((\mathbf{r}_S - \mathbf{r}_C) \cdot (\mathbf{r}_E - \mathbf{r}_C) / (|\mathbf{r}_S - \mathbf{r}_C|\,|\mathbf{r}_E - \mathbf{r}_C|)\right)$ is the angle between line segment $|SC|$ and $|EC|$, $P_n(x)$ are Legendre polynomials. Substituting (12) into (8), one can obtain 1st-order electrical potential model $\widetilde{U}^{(1)}(\mathbf{r}_E)$. Using (9), we can also yield transient potential spatial propagation model $\widetilde{u}^{(1)}(\mathbf{r}_E)$ for case study 2.

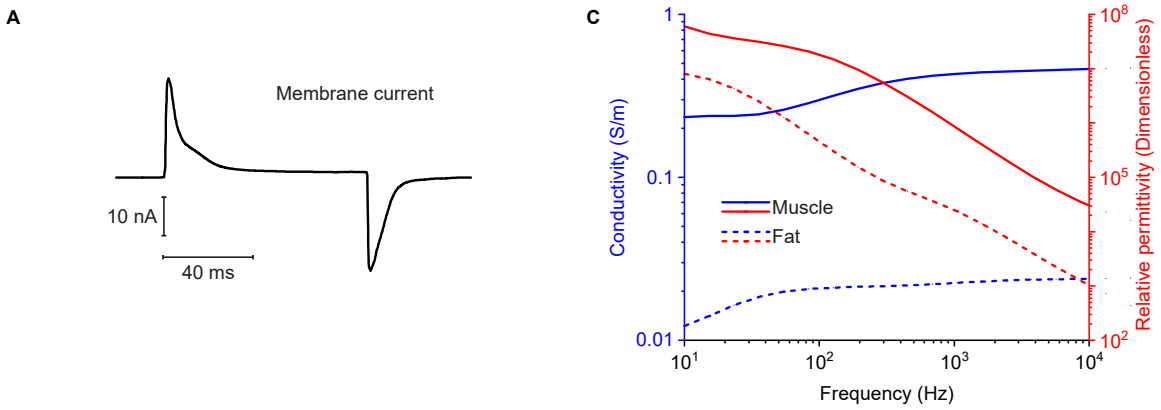

Figure 5. (A) Muscle transient current simulated. The membrane current waveform was recorded via voltage clamp in response to an 80 ms step depolarization to 0 mV from a membrane potential of -80 mV (Hernández-Ochoa & Schneider 2012). (B) Simulated conductivity (in blue color) and relative permittivity (in red color) of skeletal muscle (solid lines) and fat (dotted lines) tissue (Gabriel et al. 1996).

5. Materials and methods

5.1. Numerical potential spatial propagation

Domain Ω_1 and Ω_2 in case case study 1 and 2 are considered as skeletal muscle and fat, respectively. As shown in Figure 5 A, an experimentally recorded action current recorded by voltage clamp (Hernández-Ochoa & Schneider 2012) is considered as a current source S in Ω_1. The recording potential stimulated by sinusoidal current (I = 20 nA at 1 kHz) and membrane current (Figure 5 A) are computed in MATLAB (The Mathworks, Natick, MA, USA) using (8) and (9), respectively. The conductivity and relative permittivity of muscle and fat tissues (Figure 5 B) are obtained from an online dataset (Gabriel et al. 1996). Of note, the conductivity and relative permittivity of muscle are geometrical mean values of longitudinal and transverse electrical property in anisotropic skeletal muscle.

In case study 1, the recording electrode E is simulated in Ω_1 (Figure 6 A) and Ω_2 (Figure 6 B). Length h_{S}, h_{E} are the distances from source S, electrode E to boundary Ψ, respectively, while d_{SE} is the distance between S and E. The geometrical parameters are set as $h_{\mathrm{S}} = [1, 9]$ mm, $h_{\mathrm{E}} = [0, 10]$ mm, $d_{\mathrm{SE}} = [1, 19]$ mm. In case study 2, the recording electrode E is simulated in Ω_1 (Figure 7 A) and Ω_2 (Figure 7 B). Length R_{S}, R_{E} are the distances from source S, electrode E to spherical center C, respectively, while θ_{C} is the angle between line segment $|SC|$ and $|EC|$. The radius of spherical volume b is configured as $b = 5$ mm. Other geometrical parameters are set as $R_{\mathrm{S}} = [6, 15]$ mm, $R_{\mathrm{E}} = [0, 15]$ mm, $\theta_{\mathrm{C}} = [0°, 180°]$ mm.

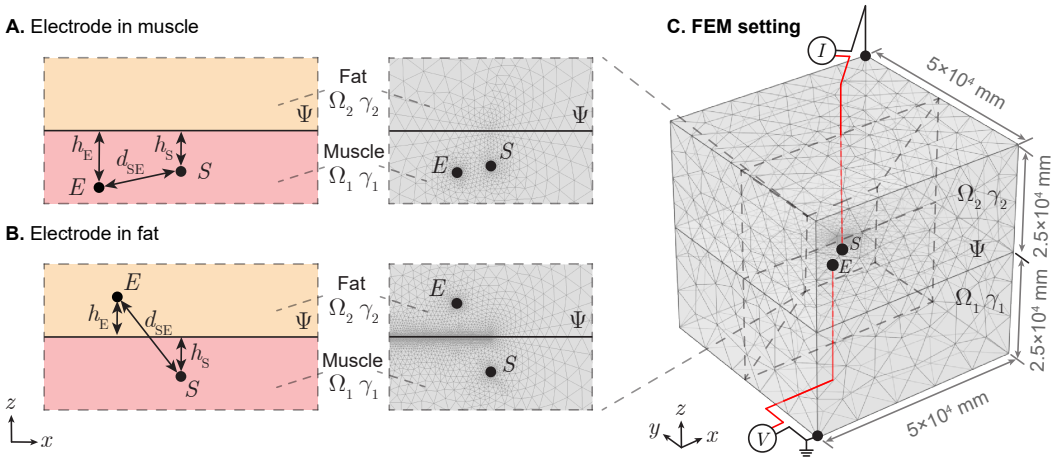

Figure 6. Illustration of case study 1 applied in needle EMG recording affected by subcutaneous fat. A plane Ψ divide full space into two half-space domains Ω_1 and Ω_2 with admittivity γ_1 and γ_2, which are configured as muscle and fat, respectively. A point-like current source S is located in muscle and potential recording electrode can be placed in skeletal muscle (A) or subcutaneous fat (B). Length h_S, h_E are the distances from point S, E to boundary Ψ, respectively, while d_{SE} is the distance between S and E. A finite element model (FEM) is built in a $5\times5\times5$ ($\times10^4$ mm) region with current sink and zero potential reference at opposite vertexs of this cube (C). The interested potential disribution area determined by source S is located in the cubic center.

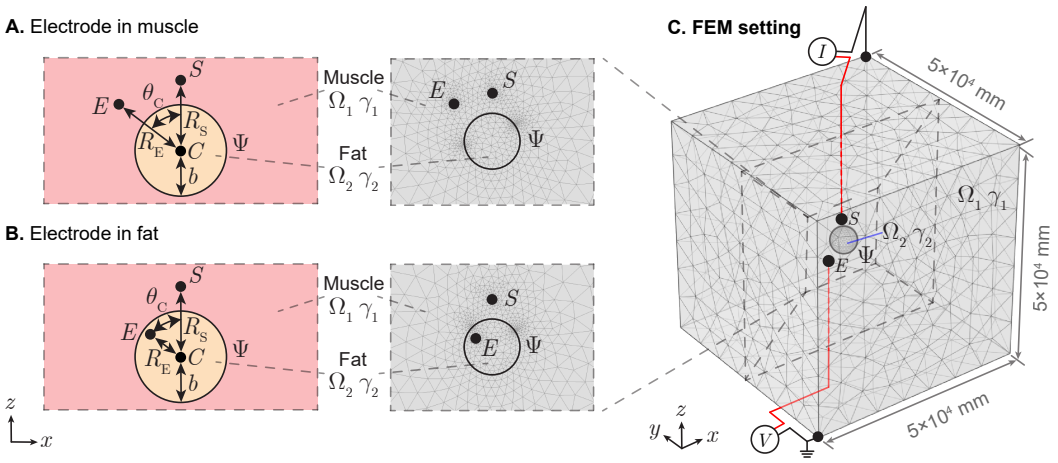

Figure 7. Application of spherical boundary case in needle EMG recording affected by intruded fat. A spherical surface Ψ divide full space into open domain Ω_1 and closed domain Ω_2 with admittivity γ_1 and γ_2, which are configured as muscle and fat, respectively. The spherical volume Ω_2 centered at point C with radius b. A point-like current source S is located in muscle and potential recording electrode can be placed in muscle (A) or fat (B). Length R_S, R_S are the distances from point S, E to C, respectively, while θ_C is the angle between line segment $|SC|$ and $|EC|$. A finite element model (FEM) is built in a $5\times5\times5$ ($\times10^4$ mm) region with current sink and zero potential reference at opposite vertexs of this cube (C). The interested potential disribution area determined by source S is in the cubic center.

5.2. Finite element model simulations

FEM simulations were performed in Comsol Multiphysics (Comsol, Inc., Burlington, MA, USA) to determine the potential spatial propagation generated by a sinusoidal current ($I = 20$ nA at 1 kHz). The simulating region was $50 \times 50 \times 50$ m^3 with current sink and zero potential reference at opposite vertexs of this cubic region (see Figure 6 C and Figure 7 C). Simultaneously, the current source S and potential recording electrode E are placed in the central area of cube, where we are interested to study the electrical potential distribution. The conductivity and the relative permittivity at 1 kHz are 4.31×10^{-1} S/m, 8.67×10^5 (dimensionless) for Ω_1, 2.25×10^{-2} S/m and 2.48×10^4 (dimensionless) for Ω_2 (Gabriel et al. 1996). Adaptive mesh was used, where the maximum and minimum mesh element size are configured as 10^3 mm and 10^{-3} mm, respectively. The maximum element growth rate is set as 1.2 and the curvature factor is 0.2. The number of degrees of freedom are 534,570 in case study 1 and 535,054 in case study 2.

6. Results

Figure 8 shows the electrical potential obtained with analytical and FEM models changing the voltage electrode position. The isopotential lines are plotted for case study 1 (Figure 8 A and E) and case study 2 (Figure 8 I and M). Unlike a homogeneous volume conductor, the distribution of potential lines are distorted by the vicinity of Ω_2 with different electrical properties than Ω_1. Also, the spacing between adjacent isopotential lines is smaller in Ω_2 than that in Ω_1. For case study 1, the magnitude and phase of the electrical potential with the voltage recording electrode in Ω_1 is shown in Figure 8 B, C, D; and Ω_2 in Figure 8 F, G, H. Similarly for case study 2, the magnitude and phase of the electrical potential with the voltage recording electrode in Ω_1 is shown in Figure 8 J, K, L; and Ω_1 in Figure 8 N, O, P. Overall, theory and FEM predicted magnitude and phase of electrical potential are in good agreement. Interestingly, when potential recording electrode is positioned in Ω_2 in case study 1 (see Figure 8 F, G, H), the phase of measured potential is a constant wherever the electrode is, and the magnitude is only determined by the distance between current source and electrode.

Figure 9 shows the electrical potential normalized by the sinusoidal current source (i.e., units of electrical impedance) changing the frequency from 10 Hz to 10 kHz, that is the frequency bandwidth of the EMG signal. Overall, the theoretical prediction does agree with FEM simulation. As expected, the frequency response of the tissue filtering characteristics is that of a low pass filter, with a minimum of the phase value at the frequency of 100 Hz.

Figure 10 illustrates the transient potential waveform excited by membrane current and recorded at different positions in case studies. The evaluating electrode can be placed in muscle and fat in case study 1 (Figure 10 A and B) and in case study 2 (Figure 10 C and D). respectively. As expected, the waveform amplitude decreases with

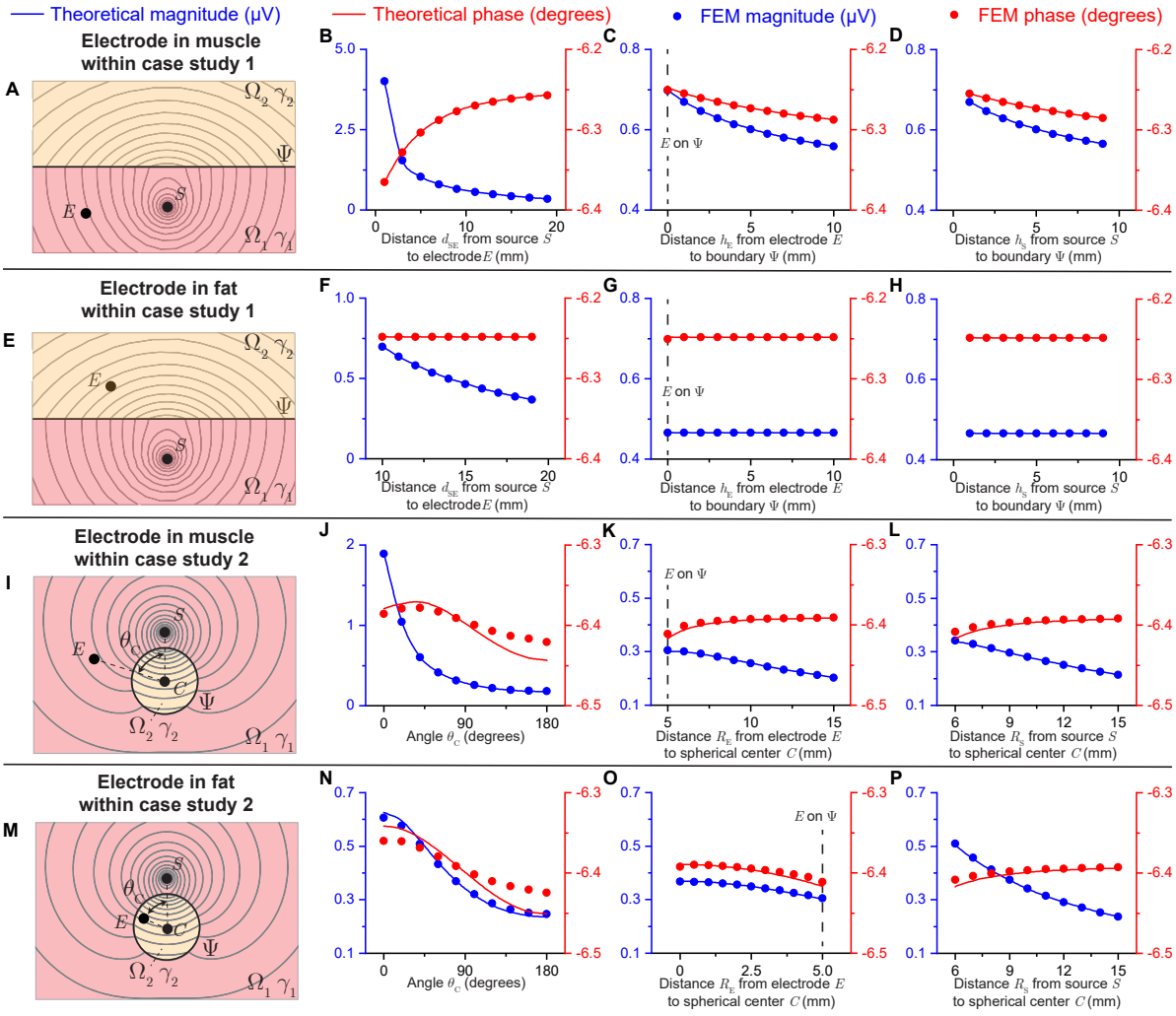

Figure 8. Analytical and FEM-simulated electrical potential results of case study 1 (see Figure 6) and case study 2 (see Figure 7) varying the electrodes position with sinusoidal current ($I = 20$ nA at 1 kHz) source. Panels (A, E, I, M) show the resultant isopotential lines in case study 1 and 2 with the source S in Ω_1 and the electrode E in Ω_1 and Ω_2. The magnitude (in blue) and phase (in red) of electrical potential are compared between theoretical prediction (solid line) and FEM simulation (circles) changing $d_{SE} = [1, 19]$ mm (B), $h_E = [0, 10]$ mm (C), $h_S = [1, 9]$ mm (D) with $d_{SE} = 10$ mm, $h_E = h_S = 5$ mm when the electrode E is in muscle for case study 1; changing $d_{SE} = [10, 19]$ mm (F), $h_E = [0, 10]$ mm (G), $h_S = [1, 9]$ mm (H) with $d_{SE} = 15$ mm, $h_E = h_S = 5$ mm when the electrode E is in fat for case study 1 (i.e., (8) with geometrical parameter (10)); changing $\theta_C = [0°, 180°]$ (J), $R_E = [5, 15]$ mm (K), $R_S = [6, 15]$ mm (L) with $\theta_C = 90°$, $R_E = 8$ mm, $R_S = 10$ mm, $b = 5$ mm when the electrode E is in muscle for case study 2; changing $\theta_C = [0°, 180°]$ (N), $R_E = [0, 5]$ mm (O), $R_S = [6, 15]$ mm (P) with $\theta_C = 90°$, $R_E = 3$ mm, $R_S = 10$ mm, $b = 5$ mm when the electrode E is in muscle for case study 2 (i.e., (8) with geometrical parameter (12)).

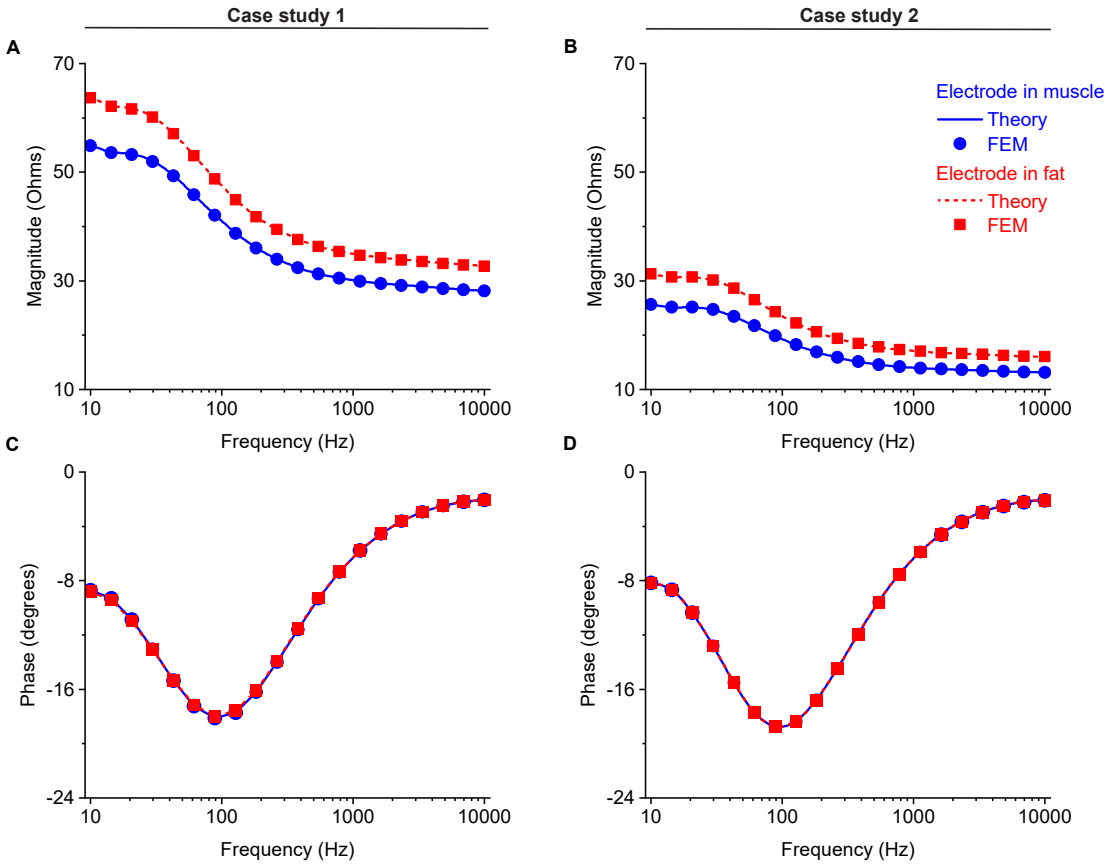

Figure 9. Analytical (solid and dotted lines) and finite element model (circles and squares) magnitude (A and B for case study 1 and 2, respectively) and phase (C and D for case study 1 and 2, respectively) of filter impedance calculated as the ratio of recorded potential to current from 10 Hz to 10 kHz. The potential recording electrode E is considered to be placed in muscle (in blue) and fat (in red). Simulation setting: (8) with geometrical parameters (10) and (12) in the frequency domain. Additional simulation parameters are: $h_{\mathrm{SE}} = 10$ mm, $h_{\mathrm{E}} = 5$ mm, $h_{\mathrm{S}} = 5$ mm, $b = 5$ mm, $R_{\mathrm{S}} = 10$ mm, $\theta_{\mathrm{C}} = 90°$, $R_{\mathrm{E}} = 8$ when the electrode is in muscle, $R_{\mathrm{E}} = 3$ mm when the electrode is in fat.

distance from recording electrode to current source. However, the waveform recorded in muscle attenuates faster than that in fat.

7. Discussion

This paper provides a framework to model monopolar EMG recordings in a nonhomogeneous conductor volume. The key contribution of our approach is that it is geometrically generic to model a changing distance between the current source and the voltage recording electrode. The framework (6) is based on perturbation theory, where the reflection coefficient Γ acts as the perturbation parameters. We then apply the first order approximation of our model (8) to study the nonhomogeneous potential spatial propagation. We analyzed the electrical potential distribution and confirmed

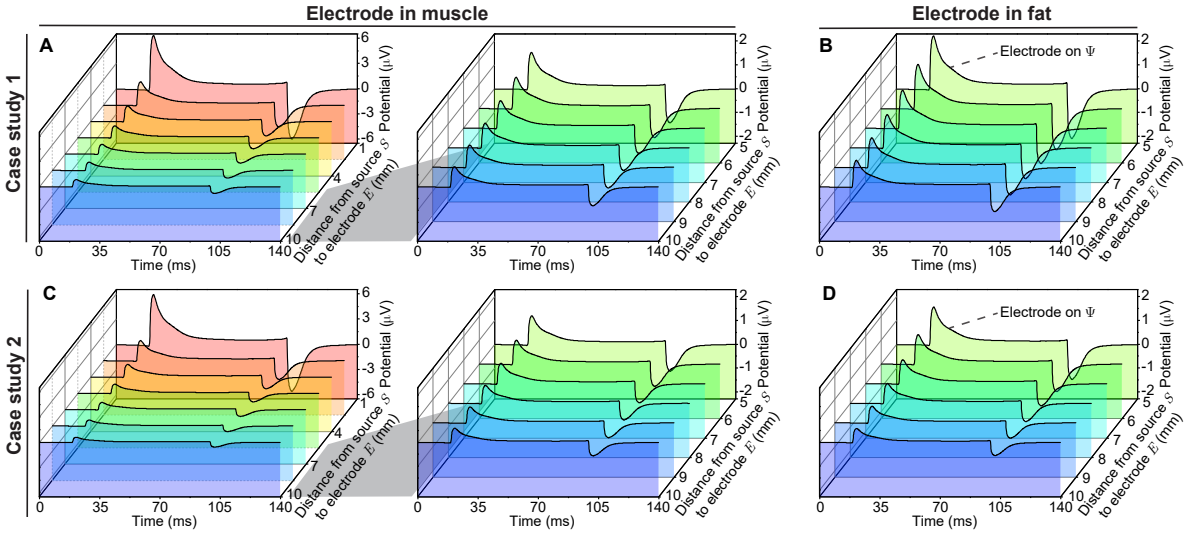

Figure 10. Simulated electrical potential propagation in nonhomogeneous muscle varying the distance from the potential recording electrode E to the current source S. The transmembrane current waveform (see Figure 5 A) is injected at S in case study 1 with the electrode E in muscle and $h_{\mathrm{E}} = h_{\mathrm{S}} + d_{\mathrm{SE}}$ mm (A), also when the electrode E is in fat with $h_{\mathrm{E}} = d_{\mathrm{SE}} - h_{\mathrm{S}}$ (B). In case study 2, the electrode E is in muscle with $R_{\mathrm{E}} = R_{\mathrm{S}} + d_{\mathrm{SE}}$ (C) and fat with $R_{\mathrm{E}} = R_{\mathrm{S}} - d_{\mathrm{SE}}$ (D). Simulation setting: (9) with geometrical parameters (10) and (12) in time domain. Additional simulation parameters: $h_{\mathrm{S}} = 5$ mm, $b = 5$ mm, $R_{\mathrm{S}} = 10$ mm, $\theta_{\mathrm{C}} = 0°$.

the usefulness of our framework performing numerical and FEM simulations in two simplified cases considering a planar and spherical boundary between muscle and fat. We found the accuracy of our theoretical predictions is dependent on Γ, namely the difference between muscle and fat electrical properties. We validated the accuracy to be $\leq 0.5\%$ even when with tissue properties differing by two orders of magnitude (Sanchez et al. 2020, Nagy et al. 2019) (Supplementary information).

Our work extends the existing scientific knowledge by modeling the effect of changing the distance between current source and electrode affecting LFPs in a nonhomogeneous measurement including the frequency-dependence of both tissues' electrical properties conductivity and permittivity. There are also several additional observations worth discussing. Of note, if one simplifies the curvature of the boundary between domains to a plane (and neglects the permittivity property), our framework provides the same potential model as the principle of image charges used in (Ness et al. 2015). Also, if one assumes the conductivity is zero and the permittivity equals vacuum permittivity in one of the domains, then our framework equips the reader with the electrical potential distribution within a finite, homogeneous, isotropic, arbitrary volume surrounded by vacuum. In this case, if the boundary surface is a plane, our framework then provides the well known electrical potential in a half space domain.

Our work has several limitations. First, the framework developed assumes the current sources are point-like. In practice, motor unit in skeletal muscle has finite size which can be modeled as a "moving" point (Duchene & Hogrel 2000), line source

(Stegeman et al. 2000), curved fiber (Roth & Beaudoin 2003) and other specific geometries (Merletti, Conte, Avignone & Guglielminotti 1999, Merletti, Roy, Kupa, Roatta & Granata 1999, Farina & Merletti 2001). Of note, our framework can be extended to model a line source using multiple discrete point-like sources with delaying waveform to consider the dimension (length) of the muscle fiber. Another limitation is the fact that the size of EMG recording electrode is not considered (Moffitt & McIntyre 2005). Further, the tissues' electrical properties are assumed to be isotropic, i.e., the same in all directions, whereas muscle is known to be anisotropic. In general, these are spatially-dependent as in the case of fusiform muscle with different values along and perpendicular to the major myofiber direction (Nagy et al. 2019). To account for this simplification in our framework, the anisotropic dependence is calculated in an average sense based on the geometrical mean of longitudinal and transverse electrical properties (Kwon et al. 2017, Kwon, Guasch, Nagy, Rutkove & Sanchez 2019, Kwon, de Morentin, Nagy, Rutkove & Sanchez 2019). Also, our model assumes that the electrical properties do not change within the tissues considered while a more realistic model will also include this spatial dependency. However, to the best of our knowledge, the authors are not aware of any experimental dataset available that has measured the spatial dependence of the electrical properties in diseased muscle. Finally, the framework only contemplates a domain model including two tissues and therefore the number of boundaries is limited to one. We are currently working to circumvent this limitation and extend the framework to model multiple nonhomogeneities with a larger number of tissues within the domain.

Despite these limitations, this work allows the reader to gain physical understanding on volume conduction mechanisms in nonhomogeneous domains affecting monopolar EMG recordings. Here, we have focused mainly on the (passive) volume conduction electrical properties of the bulk of the muscle and the effects on a measured LFPs using an intramuscular electrode. Our results provide some initial insights into how the deposition of fat within the muscle, a common sequela of many neuromuscular disorders, may impact the observed electrical potentials. Modeling a prototypical membrane current waveform, our predictions suggest an increase (amplification) of the recorded voltage. Extending our analyses to include transmembrane current waveforms as seen in neuromuscular disorders is an obvious next step to this initial work.

Conflict of interest

Dr. Sanchez holds equity in Haystack Diagnostics, a company that develops clinical needle impedance technology for neuromuscular evaluation. The company has an option to license patented needle impedance technology where the author is named an inventor. He also holds equity and serves as Scientific Advisory Committee Member of Ioniq Sciencies, a company that develops clinical impedance technology for early cancer detection. Dr. Sanchez holds equity and serves as Scientific Advisor To The Board of B-Secur, a company that develops ECG and bioimpedance technology. He consults for Myolex, Inc., a company that develops surface impedance technology. The

company has an option to license patented surface EIM technology where the author is named an inventor. Dr. Sanchez also serves as a consultant to Impedimed, a company that develops clinical impedance technology, and Texas Instruments, Happy Health, and Analog Devices, companies that develop impedance technology for consumer use.

Acknowledgment

This work was funded by the China Scholarship Council grant 201906020024 (XL) and National Institutes of Health grant R41 NS112029-01A1 (BS).

8. References

Blok J H, Stegeman D F & Van Oosterom A 2002 *Annals of biomedical engineering* **30**(4), 566–577.

Cohl H S & Tohline J E 1999 *The astrophysical journal* **527**(1), 86.

de Morentin M M, Kwon H, Pulido H V G, Nagy J A, Rutkove S B & Sanchez B 2021 *IEEE Transactions on Biomedical Engineering* .

Duchene J & Hogrel J Y 2000 *IEEE transactions on biomedical engineering* **47**(2), 192–201.

Dumitru D & Delisa J A 1991 *Muscle & Nerve: Official Journal of the American Association of Electrodiagnostic Medicine* **14**(7), 605–624.

Farina D & Merletti R 2001 *IEEE transactions on biomedical engineering* **48**(6), 637–646.

Fukada S i, Morikawa D, Yamamoto Y, Yoshida T, Sumie N, Yamaguchi M, Ito T, Miyagoe-Suzuki Y, Takeda S, Tsujikawa K et al. 2010 *The American journal of pathology* **176**(5), 2414–2424.

Gabriel S, Lau R & Gabriel C 1996 *Physics in medicine & biology* **41**(11), 2251.

He J H 1999 *International journal of non-linear mechanics* **34**(4), 699–708.

Hernández-Ochoa E O & Schneider M F 2012 *Progress in biophysics and molecular biology* **108**(3), 98–118.

Katirji B 2014 *in* 'Neuromuscular Disorders in Clinical Practice' Springer pp. 3–20.

Kwon H, de Morentin M M, Nagy J, Rutkove S & Sanchez B 2019 *Physiological measurement* **40**(8), 085008.

Kwon H, Guasch M, Nagy J, Rutkove S & Sanchez B 2019 *Scientific reports* **9**(1), 1–16.

Kwon H, Nagy J, Taylor R, Rutkove S & Sanchez B 2017 *Physics in Medicine & Biology* **62**(22), 8616.

Lowery M M, Stoykov N S, Dewald J P & Kuiken T A 2004 *IEEE Transactions on Biomedical Engineering* **51**(12), 2138–2147.

Lowery M M, Stoykov N S, Taflove A & Kuiken T A 2002 *IEEE Transactions on Biomedical Engineering* **49**(5), 446–454.

Machida M, Yamada T & Kimura J 1983 *Nihon Seikeigeka Gakkai Zasshi* **57**(3), 271–284.

Maxwell J C 1873 *A treatise on electricity and magnetism* Oxford: Clarendon Press.

Merletti R, Conte L L, Avignone E & Guglielminotti P 1999 *IEEE transactions on biomedical engineering* **46**(7), 810–820.

Merletti R, Roy S H, Kupa E, Roatta S & Granata A 1999 *IEEE Transactions on biomedical engineering* **46**(7), 821–829.

Mesin L 2013*a* *Computers in biology and medicine* **43**(7), 953–961.

Mesin L 2013*b* *Computers in biology and medicine* **43**(7), 942–952.

Mesin L & Farina D 2004 *IEEE transactions on biomedical engineering* **51**(9), 1521–1529.

Miceli S, Ness T V, Einevoll G T & Schubert D 2017 *Eneuro* **4**(1).

Moffitt M A & McIntyre C C 2005 *Clinical neurophysiology* **116**(9), 2240–2250.

Nagy J, DiDonato C, Rutkove S & Sanchez B 2019 *Scientific data* **6**(1), 1–11.

Ness T V, Chintaluri C, Potworowski J, Łęski S, Głąbska H, Wójcik D K & Einevoll G T 2015 *Neuroinformatics* **13**(4), 403–426.

Roth B J & Beaudoin D L 2003 *Physical Review E* **67**(5), 051925.
Sanchez B, Martinsen O G, Freeborn T J & Furse C M 2020 *Clinical Neurophysiology* .
Sanchez B & Rutkove S B 2017 *Neurotherapeutics* **14**(1), 107–118.
Stegeman D F, Blok J H, Hermens H J & Roeleveld K 2000 *Journal of Electromyography and Kinesiology* **10**(5), 313–326.
Wazwaz A M 2007 *Computers & Mathematics with Applications* **54**(7-8), 926–932.
Yamada T, Machida M & Kimura J 1982 *Neurology* **32**(10), 1151–1151.

Supplementary information for

Nonhomogeneous volume conduction effects affecting needle electromyography: an analytical and simulation study

Xuesong Luo[1,3], Shaoping Wang[1], Seward B. Rutkove[2] and Benjamin Sanchez[3] ‡

[1]Department of Automation Science and Electric Engineering, Beijing Advanced Innovation Center for Big Data-Based Precision Medicine, Beihang University, Beijing 100083, China.
[2]Department of Neurology, Beth Israel Deaconess Medical Center, Harvard Medical School, Boston, MA 02215, USA.
[3]Sanchez Research Lab, Department of Electrical and Computer Engineering, University of Utah, Salt Lake City, UT 84112-9206, USA.

E-mail: benjamin.sanchez@utah.edu

This PDF file includes Supplementary Parts A, B and C.

‡ Corresponding author: Dr. Benjamin Sanchez, Sorenson Molecular Biotechnology Building, Office 3721, 36 South Wasatch Drive, University of Utah, Salt Lake City, UT 84112-9206, USA, phone: (801) 585-9535, email: benjamin.sanchez@utah.edu.

Part A. Lemma 1

Surface Ψ is an infinity plane in $\mathbb{R}^3$, which divide full space into two domains Ω_1 and Ω_2. Point Q at position $\mathbf{r}_\mathrm{Q}$ is on Ψ (i.e., $\mathbf{r}_\mathrm{Q} \in \Psi$), while two different points S at $\mathbf{r}_\mathrm{S}$ and E at $\mathbf{r}_\mathrm{E}$ are arbitrarily located in $\mathbb{R}^3$ (see Figure A1 A and B). When S and E are inside the same domain, point S' at $\mathbf{r}_{\mathrm{S}'}$ is the mirrored point of S with respect to plane Ψ. Vector $\mathbf{n}_{21}(\mathbf{r}_\mathrm{Q})$ is a normal vector of surface Ψ at $\mathbf{r}_\mathrm{Q}$ pointing from Ω_2 to Ω_1. Then the 1st-order geometrical parameter $K_\Psi^{(1)}(\mathbf{r}_\mathrm{E}, \mathbf{r}_\mathrm{S})$ defined in (9) can be calculated for planar boundary as

$$
\begin{aligned}
&-\frac{1}{2\pi}\iint_\Psi \frac{\partial\left(|\mathbf{r}_\mathrm{Q}-\mathbf{r}_\mathrm{S}|\right)}{\partial \mathbf{n}_{21}(\mathbf{r}_\mathrm{Q})}\cdot\frac{\mathbf{n}_{21}(\mathbf{r}_\mathrm{Q})\,\mathrm{d}\Psi(\mathbf{r}_\mathrm{Q})}{|\mathbf{r}_\mathrm{Q}-\mathbf{r}_\mathrm{S}|^2\,|\mathbf{r}_\mathrm{E}-\mathbf{r}_\mathrm{Q}|} \\
&=\begin{cases} 0 & \text{if} \quad \mathbf{r}_\mathrm{S} \text{ on } \Psi \\ \frac{(-1)^{i-1}}{|\mathbf{r}_\mathrm{E}-\mathbf{r}_{\mathrm{S}'}|} & \text{if} \quad \mathbf{r}_\mathrm{S} \text{ and } \mathbf{r}_\mathrm{E} \text{ in } \Omega_i \\ \frac{(-1)^{i-1}}{|\mathbf{r}_\mathrm{E}-\mathbf{r}_\mathrm{S}|} & \text{else } \mathbf{r}_\mathrm{S} \text{ in } \Omega_i \text{ and } \mathbf{r}_\mathrm{E} \text{ in } \Omega_{3-i} \text{ or on } \Psi, \end{cases}
\end{aligned}
\tag{A1}
$$

where $i \in \{1, 2\}$.

Proof. Here we introduce an auxiliary model of a charged plane Ψ in vacuum to prove (A1) indirectly. Considering plane Ψ as $z = 0$ in Cartesian coordinates (x, y, z) originated at point C with coordinates $\mathbf{r}_\mathrm{C} = (0, 0, 0)$. First, we place point S on the z-axis at $\mathbf{r}_\mathrm{S} = (0, 0, z_\mathrm{S})$. Point E at $\mathbf{r}_\mathrm{E} := (0, y_{,\mathrm{E}}, z_\mathrm{E})$ is placed on the plane $x = 0$. An arbitrary point Q is placed on plane Ψ at $\mathbf{r}_\mathrm{Q} := (x, y, 0)$. Next, we assume that a charge density function $q(\mathbf{r}_\mathrm{Q}) \in \mathbb{R}$ (C m^{-2}) is distributed across the surface Ψ, defined as

$$
q(\mathbf{r}_\mathrm{Q}) := \frac{\partial\left(|\mathbf{r}_\mathrm{Q}-\mathbf{r}_\mathrm{S}|\right)}{\partial \mathbf{n}_{21}(\mathbf{r}_\mathrm{Q})}\cdot\frac{\mathbf{n}_{21}(\mathbf{r}_\mathrm{Q})}{|\mathbf{r}_\mathrm{Q}-\mathbf{r}_\mathrm{S}|^2}.
$$

The existence of $q(\mathbf{r}_\mathrm{Q})$ on the entire charged plane Ψ leads to a static electrical potential distribution $U(\mathbf{r}) \in \mathbb{R}$ (V) in $\mathbb{R}^3$. Then the static electrical potential evaluated at $\mathbf{r}_\mathrm{E}$ is deduced as

$$
U(\mathbf{r}_\mathrm{E}) = \frac{1}{4\pi\varepsilon_0}\iint_\Psi q(\mathbf{r}_\mathrm{Q})\frac{\mathrm{d}\Psi(\mathbf{r}_\mathrm{Q})}{|\mathbf{r}_\mathrm{E}-\mathbf{r}_\mathrm{Q}|},
\tag{A2}
$$

which is similar to the left hand side of (A1). Thereby, one can prove (A1) with the solution to static electrical potential $U(\mathbf{r}_\mathrm{E})$. Next, we derive the expression of $U(\mathbf{r}_\mathrm{E})$ based on (1) $\mathbf{r}_\mathrm{S}$ on Ψ (2) $\mathbf{r}_\mathrm{S}$ and $\mathbf{r}_\mathrm{E}$ in the same domain Ω_i (3) $\mathbf{r}_\mathrm{S}$ in Ω_i and $\mathbf{r}_\mathrm{E}$ in Ω_{3-i} or on Ψ .

1.1 Point S and E in the same domain

To obtain the expression of electrical potential at arbitrary position $\mathbf{r}_\mathrm{E}$, an auxiliary point E' at $\mathbf{r}_{\mathrm{E}'} := (0, 0, \mathrm{sgn}(z_\mathrm{E})R_\mathrm{E})$ on z-axis is introduced (see Figure A1 A), where $R_\mathrm{E} := |\mathbf{r}_\mathrm{E} - \mathbf{r}_\mathrm{C}|$ is the distance of line segment $|EC|$ and $\mathrm{sgn}(x)$ is the sign function. Since this model has axial symmetry with respect to z-axis, the general solution to $U(\mathbf{r}_\mathrm{E})$ then satisfies

$$
U(\mathbf{r}_\mathrm{E}) = \sum_{n=0}^{\infty}\left(A_n R_\mathrm{E}^n + \frac{B_n}{R_\mathrm{E}^{n+1}}\right)P_n(\cos\theta_\mathrm{C}),
\tag{A3}
$$

where A_n, B_n are a series of constants; $\theta_\mathrm{C} \in [0, \pi]$ (rad s^{-1}) is the angle between line segments $|SC|$ and $|EC|$; $P_n(x)$ are Legendre polynomials. When E and E' are overlap (i.e., $\theta_\mathrm{C} = 0$),

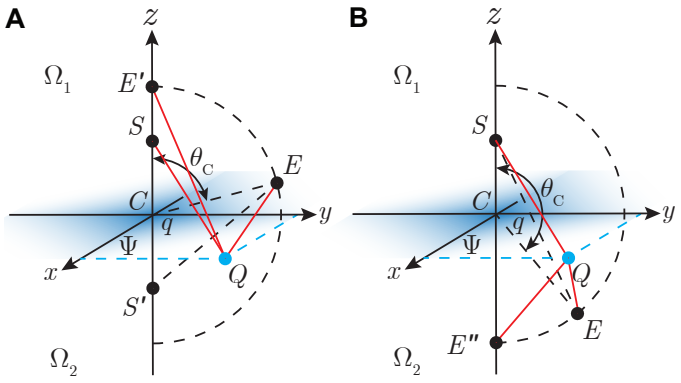

Figure A1. Auxiliary model of charged plane $\Psi : z = 0$ in vacuum. Boundary Ψ divide $\mathbb{R}^3$ into two domains $\Omega_1 : z \geq 0$ and $\Omega_2 : z \leq 0$. Position S with coordinates $\mathbf{r}_S := (0, 0, z_S)$ is on the positive z-axis of the Cartesian coordinates originated at point C. The position Q has coordinates $\mathbf{r}_Q := (x, y, 0)$ is an arbitrary point on plane Ψ. The charge density $q(\mathbf{r}_Q)$ is distributed on Ψ. Positions E, E' and E'' are three points on the plane $x = 0$, which satisfy the line segments $|EC| = |E'C| = |E''C|$. Point E' is on the positive z-axis (A) while E'' is on the negative z-axis (B). Angle θ_C is the angle between line segments $|SC|$ and $|EC|$. Point S' at $(0, 0, -z_S)$ is a mirrored point of S with respect to Ψ in (A).

then (A3) is rewritten as

$$U(\mathbf{r}_{E'}) = \sum_{n=0}^{\infty} \left(A_n R_E^n + \frac{B_n}{R_E^{n+1}} \right). \tag{A4}$$

According to (A2) in Cartesian coordinates, electrical potential at E' can also be expressed as

$$U\left(\mathbf{r}_{E'}\right) = \frac{1}{4\pi\varepsilon_0} \int_{-\infty}^{\infty} \int_{-\infty}^{\infty} -\frac{\partial R_{SQ}}{\partial z_S} \frac{\mathrm{d}x\mathrm{d}y}{R_{SQ}^2 R_{QE'}}, \tag{A5}$$

in which $R_{SQ} := |\mathbf{r}_Q - \mathbf{r}_S| = \sqrt{x^2 + y^2 + z_S^2}$ is the distance between S and Q; $R_{QE'} := |\mathbf{r}_{E'} - \mathbf{r}_Q| = \sqrt{x^2 + y^2 + R_E^2}$ is the distance between Q and E'. Equation (A5) can be further simplified as

$$U\left(\mathbf{r}_{E'}\right) = -\frac{\mathrm{sgn}(z_S)}{2\varepsilon_0} \frac{1}{|z_S| + R_E}. \tag{A6}$$

When $|z_S| \neq R_E$, (A6) can be rewritten using Taylor series as

$$U\left(\mathbf{r}_{E'}\right) = \begin{cases} -\frac{\mathrm{sgn}(z_S)}{2\varepsilon_0 R_E} \sum_{n=0}^{\infty} \left(-\frac{|z_S|}{R_E} \right)^n & \text{if } R_E > |z_S| \\ -\frac{\mathrm{sgn}(z_S)}{2\varepsilon_0 |z_S|} \sum_{n=0}^{\infty} \left(-\frac{R_E}{|z_S|} \right)^n & \text{if } R_E < |z_S|. \end{cases} \tag{A7}$$

Comparing (A7) with (A4) we have

$$\begin{cases} A_n = 0,\ B_n = -\frac{\mathrm{sgn}(z_S)}{2\varepsilon_0} \left(-|z_S|\right)^n & \text{if } R_E > |z_S| \\ A_n = \frac{\mathrm{sgn}(z_S)}{2\varepsilon_0} \left(-|z_S|\right)^{-n-1},\ B_n = 0 & \text{if } R_E < |z_S|. \end{cases} \tag{A8}$$

Then, the Legendre polynomials can also be written as

$$\frac{1}{\sqrt{x^2 - 2xt + 1}} = \sum_{n=0}^{\infty} x^n P_n\left(t\right), \tag{A9}$$

which we can plug into (A3) using (A8) as well to obtain

$$U(\mathbf{r}_{\mathrm{E}}) = -\frac{\mathrm{sgn}(z_{\mathrm{S}})}{2\varepsilon_0\sqrt{R_{\mathrm{E}}^2 - 2R_{\mathrm{E}}|z_{\mathrm{S}}|\cos(\pi - \theta_{\mathrm{C}}) + z_{\mathrm{S}}^2}}. \tag{A10}$$

When $|z_{\mathrm{S}}| = R_{\mathrm{E}}$, then

$$U(\mathbf{r}_{\mathrm{E}})|_{|z_{\mathrm{S}}|=R_{\mathrm{E}}} \in \left[\lim_{\Delta\to 0} U(\mathbf{r}_{\mathrm{E}})|_{|z_{\mathrm{S}}|=R_{\mathrm{E}}-\Delta}, \lim_{\Delta\to 0} U(\mathbf{r}_{\mathrm{E}})|_{|z_{\mathrm{S}}|=R_{\mathrm{E}}+\Delta}\right].$$

According to (A10) and the Squeeze theorem, (A10) also satisfies that $|z_{\mathrm{S}}| = R_{\mathrm{E}}$.

As illustrated in Figure A1 A, we introduce a auxiliary point S' at $\mathbf{r}_{\mathrm{S}} = (0, 0, -z_{\mathrm{S}})$ to simplify (A10). Point S' is the mirrored image of S with respect to plane Ψ. Then the distance between S' and E is described as

$$R_{\mathrm{S'E}} := |\mathbf{r}_{\mathrm{E}} - \mathbf{r}_{\mathrm{S'}}| = \sqrt{R_{\mathrm{E}}^2 - 2R_{\mathrm{E}}|z_{\mathrm{S}}|\cos(\pi - \theta_{\mathrm{C}}) + z_{\mathrm{S}}^2}.$$

Finally, we can write the electrical potential at $\mathbf{r}_{\mathrm{E}}$ as

$$U(\mathbf{r}_{\mathrm{E}}) = -\frac{\mathrm{sgn}(z_{\mathrm{S}})}{2\varepsilon_0 R_{\mathrm{S'E}}}. \tag{A11}$$

1.2 Point E on plane Ψ or in different domain from S

To obtain the expression of electrical potential at arbitrary position $\mathbf{r}_{\mathrm{E}}$, an auxiliary point E'' at $\mathbf{r}_{\mathrm{E''}} := (0, 0, \mathrm{sgn}(z_{\mathrm{E}})R_{\mathrm{E}})$ on z-axis is introduced (see Figure A1 B). When $\theta_{\mathrm{C}} = \pi$, then (A3) is

$$U(\mathbf{r}_{\mathrm{E''}}) = \sum_{n=0}^{\infty}(-1)^n\left(A_n R_{\mathrm{E}}^n + \frac{B_n}{R_{\mathrm{E}}^{n+1}}\right). \tag{A12}$$

Replacing E' with E'' in (A6), the electrical potential at E'' can be re-written as

$$U(\mathbf{r}_{\mathrm{E''}}) = \frac{\mathrm{sgn}(z_{\mathrm{S}})}{2\varepsilon_0}\frac{1}{|z_{\mathrm{S}}| + R_{\mathrm{E}}}. \tag{A13}$$

Similar mathematical operations as (A7) (A8) (A9) (A10) can be performed to (A12) and (A13). Then we can find general expression for electrical potential $U(\mathbf{r}_{\mathrm{E}})$, namely,

$$U(\mathbf{r}_{\mathrm{E}}) = -\frac{\mathrm{sgn}(z_{\mathrm{S}})}{2\varepsilon_0\sqrt{R_{\mathrm{E}}^2 - 2R_{\mathrm{E}}|z_{\mathrm{S}}|\cos\theta_{\mathrm{C}} + z_{\mathrm{S}}^2}} = -\frac{\mathrm{sgn}(z_{\mathrm{S}})}{2\varepsilon_0 R_{\mathrm{SE}}} \tag{A14}$$

where $R_{\mathrm{SE}} := |\mathbf{r}_{\mathrm{E}} - \mathbf{r}_{\mathrm{S}}| = \sqrt{R_{\mathrm{E}}^2 - 2R_{\mathrm{E}}|z_{\mathrm{S}}|\cos\mathrm{C} + z_{\mathrm{S}}^2}$ is the distance between S and E.

1.3 Point S on plane Ψ

From the assumption we have $\mathbf{r}_{\mathrm{S}} \in \Psi$. Meanwhile according to the definition of $\mathbf{r}_{\mathrm{Q}}$, we can find that $\mathbf{r}_{\mathrm{Q}} \in \Psi$. It follows that

$$\frac{\partial\left(|\mathbf{r}_{\mathrm{Q}} - \mathbf{r}_{\mathrm{S}}|\right)}{\partial\mathbf{n}_{21}\left(\mathbf{r}_{\mathrm{Q}}\right)} \equiv 0.$$

According to (A2) we have

$$U(\mathbf{r}_{\mathrm{E}}) \equiv 0. \tag{A15}$$

One can find (A1) equating the right hand sides of (A11), (A14), (A15) and (A2).

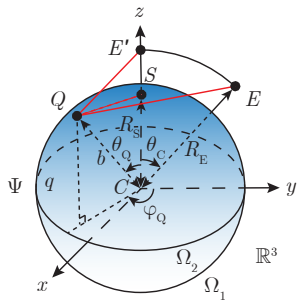

Figure B1. Auxiliary model of charged spherical shell in vacuum. A nonuniform charged spherical shell Ψ is centered at the origin C of spherical coordinates (r, θ, φ) in infinity vacuum $\mathbb{R}^3$ with b the radius of Ψ. Boundary Ψ divide the full space into two domains $\Omega_1 : r \geq b$ and $\Omega_2 : r \leq b$. The position Q has coordinates $\mathbf{r}_{\mathrm{Q}} := (b, \theta_{\mathrm{Q}}, \varphi_{\mathrm{Q}})$ on Ψ. The charge density $q(\mathbf{r}_{\mathrm{Q}})$ is distributed on surface Ψ. The position S, E and E' have coordinates $\mathbf{r}_{\mathrm{S}} := (R_{\mathrm{S}}, 0, 0)$, $\mathbf{r}_{\mathrm{E}} := (R_{\mathrm{E}}, \theta_{\mathrm{C}}, 0)$ and $\mathbf{r}_{\mathrm{E}'} := (R_{\mathrm{E}}, 0, 0)$, which satisfy $|EC| = |E'C|$ and S, E' are on positive z-axis. The length R_{S} is the distance between S and C; the length R_{E} is the distance between E and C. The angle θ_{C} is defined between line segment $|SC|$ and $|EC|$; θ_{Q} is the angle between line segment $|SC|$ and $|EC|$.

Part B. Lemma 2

Surface Ψ is a spherical surface centered at C with radius b in $\mathbb{R}^3$, which divide the full space into two domains Ω_1 and Ω_2. Point Q at position $\mathbf{r}_{\mathrm{Q}}$ is on Ψ (i.e., $\mathbf{r}_{\mathrm{Q}} \in \Psi$), while two different points S at $\mathbf{r}_{\mathrm{S}}$ and E at $\mathbf{r}_{\mathrm{E}}$ are arbitrarily located in $\mathbb{R}^3$ (see Figure B1). Vector $\mathbf{n}_{21}(\mathbf{r}_{\mathrm{Q}})$ is a normal vector of surface Ψ at $\mathbf{r}_{\mathrm{Q}}$ pointing from Ω_2 to Ω_1. R_{S} and R_{E} are are the distance between S and C, E and C, respectively. Then the 1st-order geometrical parameter $K_{\Psi}^{(1)}(\mathbf{r}_{\mathrm{E}}, \mathbf{r}_{\mathrm{S}})$ defined in (9) can be calculated as

$$-\frac{1}{2\pi}\iint_{\Psi}\frac{\partial\left(|\mathbf{r}_{\mathrm{Q}}-\mathbf{r}_{\mathrm{S}}|\right)}{\partial\mathbf{n}_{21}(\mathbf{r}_{\mathrm{Q}})}\cdot\frac{\mathbf{n}_{21}(\mathbf{r}_{\mathrm{Q}})\,\mathrm{d}\Psi(\mathbf{r}_{\mathrm{Q}})}{|\mathbf{r}_{\mathrm{Q}}-\mathbf{r}_{\mathrm{S}}|^2\,|\mathbf{r}_{\mathrm{E}}-\mathbf{r}_{\mathrm{Q}}|} \tag{B1}$$

$$= \begin{cases} \frac{b}{R_{\mathrm{S}}R_{\mathrm{E}}}\sum_{n=0}^{\infty}\frac{2n}{2n+1}\left(\frac{b^2}{R_{\mathrm{S}}R_{\mathrm{E}}}\right)^n P_n(\cos\theta_{\mathrm{C}}) & \text{if} \quad R_{\mathrm{S}} > b, R_{\mathrm{E}} \geq b \\ \frac{1}{R_{\mathrm{S}}}\sum_{n=0}^{\infty}\frac{2n}{2n+1}\left(\frac{R_{\mathrm{E}}}{R_{\mathrm{S}}}\right)^n P_n(\cos\theta_{\mathrm{C}}) & \text{if} \quad R_{\mathrm{S}} > b, R_{\mathrm{E}} \leq b \\ -\frac{1}{R_{\mathrm{E}}}\sum_{n=0}^{\infty}\frac{1}{2n+1}\left(\frac{b}{R_{\mathrm{E}}}\right)^n P_n(\cos\theta_{\mathrm{C}}) & \text{if} \quad R_{\mathrm{S}} = b, R_{\mathrm{E}} \geq b \\ -\frac{1}{b}\sum_{n=0}^{\infty}\frac{1}{2n+1}\left(\frac{R_{\mathrm{E}}}{b}\right)^n P_n(\cos\theta_{\mathrm{C}}) & \text{if} \quad R_{\mathrm{S}} = b, R_{\mathrm{E}} \leq b \\ -\frac{1}{R_{\mathrm{E}}}\sum_{n=0}^{\infty}\frac{2n+2}{2n+1}\left(\frac{R_{\mathrm{S}}}{R_{\mathrm{E}}}\right)^n P_n(\cos\theta_{\mathrm{C}}) & \text{if} \quad R_{\mathrm{S}} < b, R_{\mathrm{E}} \geq b \\ -\frac{1}{b}\sum_{n=0}^{\infty}\frac{2n+2}{2n+1}\left(\frac{R_{\mathrm{S}}R_{\mathrm{E}}}{b^2}\right)^n P_n(\cos\theta_{\mathrm{C}}) & \text{else } R_{\mathrm{S}} < b, R_{\mathrm{E}} \leq b. \end{cases} \tag{B2}$$

Proof. Firstly, we establish a spherical coordinates in $\mathbb{R}^3$ originated at the center C of spherical surface Ψ. The position $\mathbf{r} := (r, \theta, \varphi)$ is defined in spherical coordinates. For convenience, we consider S with coordinates $\mathbf{r}_{\mathrm{S}} := (R_{\mathrm{S}}, 0, 0)$ on the positive z-axis, while E with coordinates $\mathbf{r}_{\mathrm{E}} := (R_{\mathrm{E}}, \theta_{\mathrm{C}}, 0)$ is placed on the plane $\varphi = 0$. Point Q with coordinates $\mathbf{r}_{\mathrm{Q}} := (b, \theta_{\mathrm{Q}}, \varphi_{\mathrm{Q}})$ is an arbitrary point on Ψ. Angle θ_{C} is the angle between line segment $|SC|$ and $|EC|$, θ_{Q} is the angle between line segment $|SC|$ and $|QC|$. Next, we follow a similar procedure as we did in Lemma 1, proving (B2) indirectly with an auxiliary physical model of charged spherical surface Ψ in vacuum.

2.1 Neither point S nor E is on spherical surface Ψ

Considering a charge density function $q(\mathbf{r}_{\mathrm{Q}})$ on the spherical surface Ψ, as illustrated in Figure B1, we already know the electrical potential $U(\mathbf{r}_{\mathrm{E}})$ is the key to give the proof from Lemma 1. Introduce an auxiliary point E' with coordinates $\mathbf{r}_{\mathrm{E}'} := (R_{\mathrm{E}}, 0, 0)$ on positive z-axis, which satisfy $|E'C| = |EC|$. From (A2), $U(\mathbf{r}_{\mathrm{E}'})$ can be expressed as

$$U(\mathbf{r}_{\mathrm{E}'}) = \frac{1}{4\pi\varepsilon_0}\int_{-\pi}^{\pi}\int_{0}^{\pi}\frac{\partial\left(|\mathbf{r}_{\mathrm{Q}}-\mathbf{r}_{\mathrm{S}}|\right)}{\partial b}\frac{b^2\sin\theta_{\mathrm{Q}}\mathrm{d}\theta_{\mathrm{Q}}\mathrm{d}\varphi_{\mathrm{Q}}}{|\mathbf{r}_{\mathrm{Q}}-\mathbf{r}_{\mathrm{S}}|^2\,|\mathbf{r}_{\mathrm{E}'}-\mathbf{r}_{\mathrm{Q}}|} \tag{B3}$$

where $|\mathbf{r}_{\mathrm{Q}}-\mathbf{r}_{\mathrm{S}}| = \sqrt{R_{\mathrm{S}}^2+b^2-2bR_{\mathrm{S}}\cos\theta_{\mathrm{Q}}}$ and $|\mathbf{r}_{\mathrm{E}'}-\mathbf{r}_{\mathrm{Q}}| = \sqrt{R_{\mathrm{E}}^2+b^2-2bR_{\mathrm{E}}\cos\theta_{\mathrm{Q}}}$. Equation (B3) can be further simplified as

$$U(\mathbf{r}_{\mathrm{E}'}) = \begin{cases} \frac{1}{4\varepsilon_0}\left(\frac{2b}{b^2-R_{\mathrm{S}}R_{\mathrm{E}}}+\frac{1}{\sqrt{R_{\mathrm{S}}R_{\mathrm{E}}}}\ln\left(\frac{\sqrt{R_{\mathrm{S}}R_{\mathrm{E}}}+b}{\sqrt{R_{\mathrm{S}}R_{\mathrm{E}}}-b}\right)\right) & \text{if } R_{\mathrm{S}}>b, R_{\mathrm{E}}>b \\ \frac{1}{4\varepsilon_0}\left(\frac{2}{R_{\mathrm{E}}-R_{\mathrm{S}}}+\frac{1}{\sqrt{R_{\mathrm{S}}R_{\mathrm{E}}}}\ln\left(\frac{\sqrt{R_{\mathrm{S}}}+\sqrt{R_{\mathrm{E}}}}{\sqrt{R_{\mathrm{S}}}-\sqrt{R_{\mathrm{E}}}}\right)\right) & \text{if } R_{\mathrm{S}}>b, R_{\mathrm{E}}<b \\ \frac{1}{4\varepsilon_0}\left(\frac{2}{R_{\mathrm{E}}-R_{\mathrm{S}}}+\frac{1}{\sqrt{R_{\mathrm{S}}R_{\mathrm{E}}}}\ln\left(\frac{\sqrt{R_{\mathrm{E}}}+\sqrt{R_{\mathrm{S}}}}{\sqrt{R_{\mathrm{E}}}-\sqrt{R_{\mathrm{S}}}}\right)\right) & \text{if } R_{\mathrm{S}}<b, R_{\mathrm{E}}>b \\ \frac{1}{4\varepsilon_0}\left(\frac{2b}{b^2-R_{\mathrm{S}}R_{\mathrm{E}}}+\frac{1}{\sqrt{R_{\mathrm{S}}R_{\mathrm{E}}}}\ln\left(\frac{b+\sqrt{R_{\mathrm{S}}R_{\mathrm{E}}}}{b-\sqrt{R_{\mathrm{S}}R_{\mathrm{E}}}}\right)\right) & \text{if } R_{\mathrm{S}}<b, R_{\mathrm{E}}<b. \end{cases} \tag{B4}$$

Expression (B4) can be rewritten using Taylor series as

$$U(\mathbf{r}_{\mathrm{E}'}) = \begin{cases} -\frac{b}{2\varepsilon_0 R_{\mathrm{S}}R_{\mathrm{E}}}\sum_{n=0}^{\infty}\frac{2n}{2n+1}\left(\frac{b^2}{R_{\mathrm{S}}R_{\mathrm{E}}}\right)^n & \text{if } R_{\mathrm{S}}>b, R_{\mathrm{E}}>b \\ -\frac{1}{2\varepsilon_0 R_{\mathrm{S}}}\sum_{n=0}^{\infty}\frac{2n}{2n+1}\left(\frac{R_{\mathrm{E}}}{R_{\mathrm{S}}}\right)^n & \text{if } R_{\mathrm{S}}>b, R_{\mathrm{E}}<b \\ \frac{1}{2\varepsilon_0 R_{\mathrm{E}}}\sum_{n=0}^{\infty}\frac{2n+2}{2n+1}\left(\frac{R_{\mathrm{S}}}{R_{\mathrm{E}}}\right)^n & \text{if } R_{\mathrm{S}}<b, R_{\mathrm{E}}>b \\ \frac{1}{2\varepsilon_0 b}\sum_{n=0}^{\infty}\frac{2n+2}{2n+1}\left(\frac{R_{\mathrm{S}}R_{\mathrm{E}}}{b^2}\right)^n & \text{if } R_{\mathrm{S}}<b, R_{\mathrm{E}}<b. \end{cases} \tag{B5}$$

Comparing (B5) and (A4), we have

$$\begin{cases} A_n = 0, B_n = -\frac{1}{2\varepsilon_0}\frac{2n}{2n+1}\frac{b^{2n+1}}{R_{\mathrm{S}}^{n+1}} & \text{if } R_{\mathrm{S}}>b, R_{\mathrm{E}}>b \\ A_n = -\frac{1}{2\varepsilon_0}\frac{2n}{2n+1}\frac{1}{R_{\mathrm{S}}^{n+1}}, B_n = 0 & \text{if } R_{\mathrm{S}}>b, R_{\mathrm{E}}<b \\ A_n = 0, B_n = \frac{1}{2\varepsilon_0}\frac{2n+2}{2n+1}R_{\mathrm{S}}^n & \text{if } R_{\mathrm{S}}<b, R_{\mathrm{E}}>b \\ A_n = \frac{1}{2\varepsilon_0}\frac{2n+2}{2n+1}\frac{R_{\mathrm{S}}^n}{b^{2n+1}}, B_n = 0 & \text{if } R_{\mathrm{S}}<b, R_{\mathrm{E}}<b. \end{cases} \tag{B6}$$

Substituting (B6) to (A3) gives

$$U(\mathbf{r}_{\mathrm{E}}) = U(\mathbf{r}_{\mathrm{E}'})\,P_n(\cos\theta_{\mathrm{C}}). \tag{B7}$$

2.2 Either point S or E is on spherical surface Ψ Next we consider the cases when $R_{\mathrm{S}} = b$ or $R_{\mathrm{E}} = b$, which can be yield from the limit when R_{S} or R_{E} approaches b in (B7). The electrical potential on these singularity is defined as

$$U(\mathbf{r}_{\mathrm{E}}) := \begin{cases} \lim_{\Delta\to 0}\frac{U(\mathbf{r}_{\mathrm{E}})|_{R_{\mathrm{S}}=b+\Delta,R_{\mathrm{E}}>b}+U(\mathbf{r}_{\mathrm{E}})|_{R_{\mathrm{S}}=b-\Delta,R_{\mathrm{E}}>b}}{2} & \text{if } R_{\mathrm{S}}=b, R_{\mathrm{E}}>b \\ \lim_{\Delta\to 0}\frac{U(\mathbf{r}_{\mathrm{E}})|_{R_{\mathrm{S}}=b+\Delta,R_{\mathrm{E}}<b}+U(\mathbf{r}_{\mathrm{E}})|_{R_{\mathrm{S}}=b-\Delta,R_{\mathrm{E}}<b}}{2} & \text{if } R_{\mathrm{S}}=b, R_{\mathrm{E}}<b \\ \lim_{\Delta\to 0}\frac{U(\mathbf{r}_{\mathrm{E}})|_{R_{\mathrm{S}}>b,R_{\mathrm{E}}=b+\Delta}+U(\mathbf{r}_{\mathrm{E}})|_{R_{\mathrm{S}}>b,R_{\mathrm{E}}=b-\Delta}}{2} & \text{if } R_{\mathrm{S}}>b, R_{\mathrm{E}}=b \\ \lim_{\Delta\to 0}\frac{U(\mathbf{r}_{\mathrm{E}})|_{R_{\mathrm{S}}<b,R_{\mathrm{E}}=b+\Delta}+U(\mathbf{r}_{\mathrm{E}})|_{R_{\mathrm{S}}<b,R_{\mathrm{E}}=b-\Delta}}{2} & \text{if } R_{\mathrm{S}}<b, R_{\mathrm{E}}=b \\ \lim_{\Delta\to 0}\frac{U(\mathbf{r}_{\mathrm{E}})|_{R_{\mathrm{S}}=R_{\mathrm{E}}=b+\Delta}+U(\mathbf{r}_{\mathrm{E}})|_{R_{\mathrm{S}}=R_{\mathrm{E}}=b-\Delta}}{2} & \text{if } R_{\mathrm{S}}=b, R_{\mathrm{E}}=b \end{cases} \tag{B8}$$

Substituting (B5), (B7) into (B8) we have

$$U(\mathbf{r}_{\mathrm{E}}) = \begin{cases} \frac{1}{2\varepsilon_0 R_{\mathrm{E}}} \sum_{n=0}^{\infty} \frac{1}{2n+1} \left(\frac{b}{R_{\mathrm{E}}}\right)^n P_n(\cos\theta_{\mathrm{C}}) & \text{if } R_{\mathrm{S}} = b, R_{\mathrm{E}} > b \\ \frac{1}{2\varepsilon_0 b} \sum_{n=0}^{\infty} \frac{1}{2n+1} \left(\frac{R_{\mathrm{E}}}{b}\right)^n P_n(\cos\theta_{\mathrm{C}}) & \text{if } R_{\mathrm{S}} = b, R_{\mathrm{E}} < b \\ -\frac{1}{2\varepsilon_0 R_{\mathrm{S}}} \sum_{n=0}^{\infty} \frac{2n}{2n+1} \left(\frac{b}{R_{\mathrm{S}}}\right)^n P_n(\cos\theta_{\mathrm{C}}) & \text{if } R_{\mathrm{S}} > b, R_{\mathrm{E}} = b \\ \frac{1}{2\varepsilon_0 b} \sum_{n=0}^{\infty} \frac{2n+2}{2n+1} \left(\frac{R_{\mathrm{S}}}{b}\right)^n P_n(\cos\theta_{\mathrm{C}}) & \text{if } R_{\mathrm{S}} < b, R_{\mathrm{E}} = b \\ \frac{1}{2\varepsilon_0 b} \sum_{n=0}^{\infty} \frac{1}{2n+1} P_n(\cos\theta_{\mathrm{C}}) & \text{if } R_{\mathrm{S}} = b, R_{\mathrm{E}} = b. \end{cases} \tag{B9}$$

One can find (B2) equating the right hand sides of (B7), (B9) and (A2).

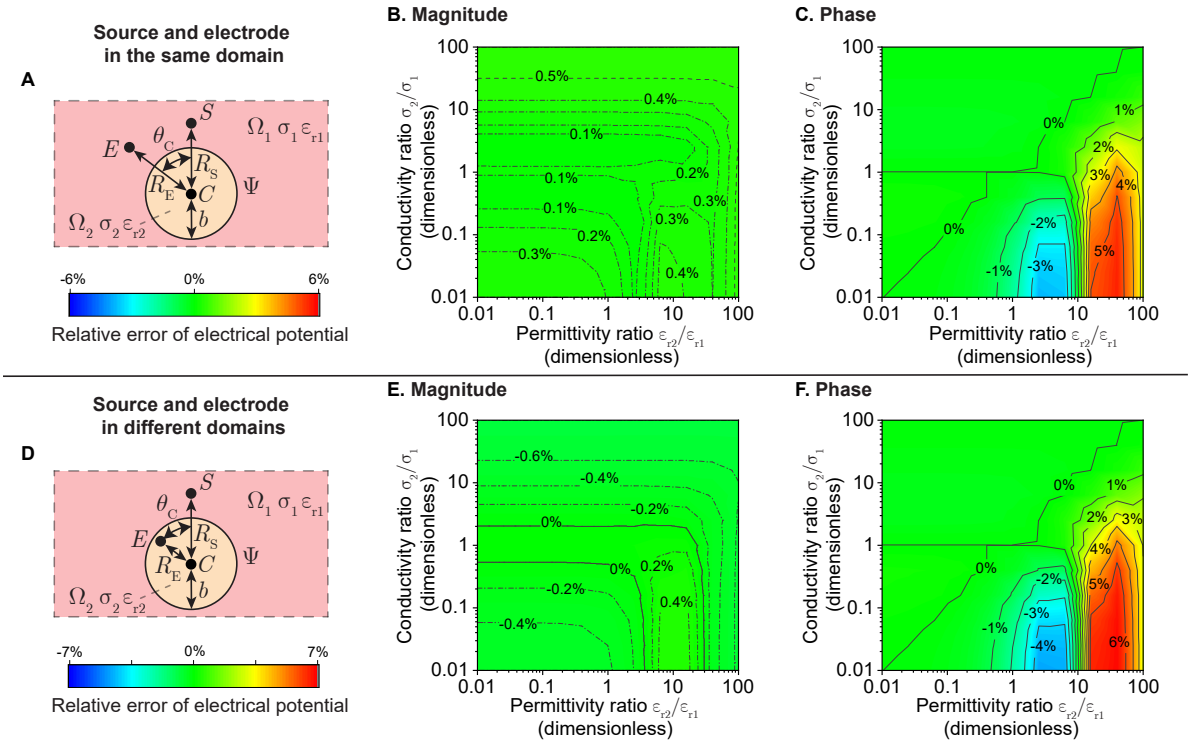

Figure B2. Relative error distribution of electrical potential between theory and FEM with varying nonhomogeneous electrical property in case study 2. A spherical surface Ψ with radius b centered at point C divides full space into two domain Ω_1 and Ω_2 with conductivity $\sigma_{\{1,2\}}$ and relative permittivity $\varepsilon_{\{\mathrm{r1,r2}\}}$, respectively. Sinusoidal current ($I = 20$ nA of 1 kHz) source S and potential recording electrode E are placed in the same domain (A) and in different domains (D). Angle θ_{C} is the angle between of line segment $|EC|$ and $|SC|$, and R_{S}, R_{E} are distance from S, E to point C, respectively. Relative error distributions of potential magnitude and phase when E in Ω_1 with $R_{\mathrm{E}} = 8$ mm (B, C) and E in Ω_2 with $R_{\mathrm{E}} = 3$ mm (E, F) changing the conductivity $\sigma_2 = [0.01 \cdot \sigma_1, 100 \cdot \sigma_1]$ and relative permittivity $\varepsilon_{\mathrm{r2}} = [0.01 \cdot \varepsilon_{\mathrm{r1}}, 100 \cdot \varepsilon_{\mathrm{r1}}]$. Additional simulation parameters: $b = 5$ mm, $R_{\mathrm{S}} = 10$ mm, $\theta_{\mathrm{C}} = 90°$, $\sigma_1 = 0.431$ S/m, $\varepsilon_1 = 8.67 \times 10^5$ (dimensionless).

Part C. Accuracy analysis

We proposed (9) to calculate the 1st-order approximated electrical potential in a nonhomogeneous conducting volume. Therefore, the accuracy of the approximation is

determined by how electrically similar or different the tissues within the domain are. Here, we compare the 1st-order approximation with finite element model simulation considering the same case study 1 and 2 to assess the accuracy when varying the tissues' electrical properties.

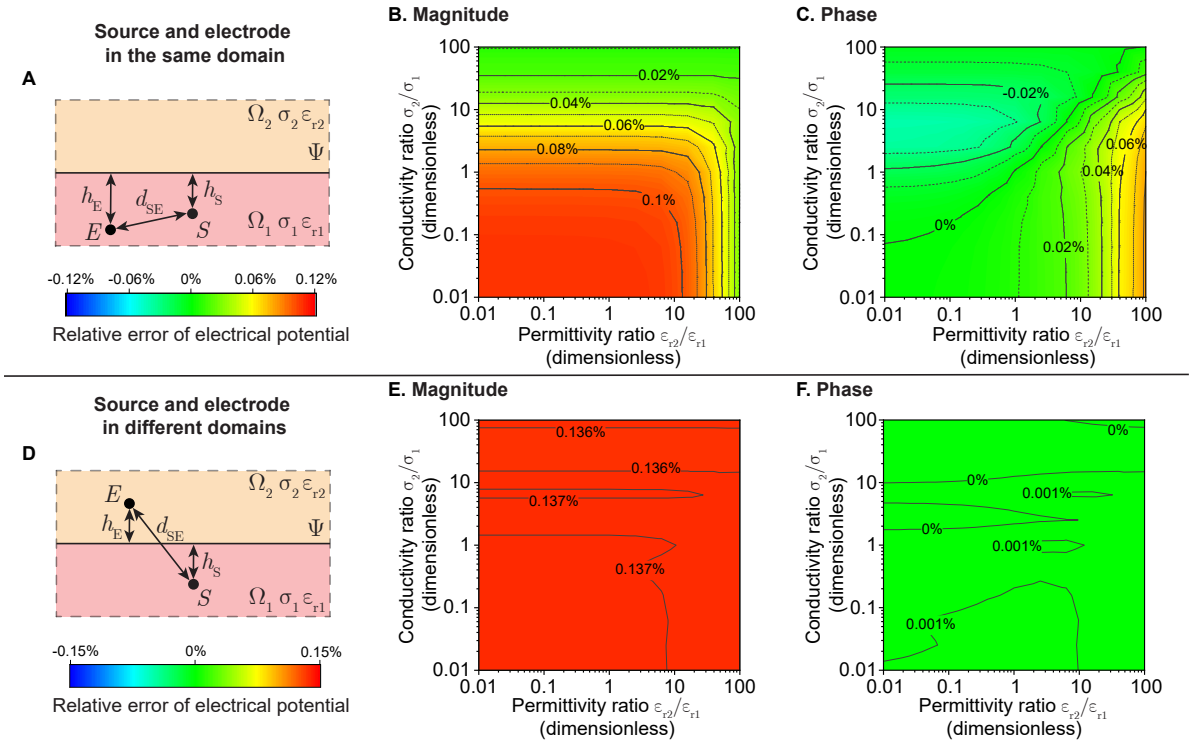

Figure C1. Relative error distribution of electrical potential between theory and FEM with varying nonhomogeneous electrical property in case study 1. A plane Ψ divides full space into two domain Ω_1 and Ω_2 with conductivity $\sigma_{\{1,2\}}$ and relative permittivity $\varepsilon_{\{\mathrm{r1,r2}\}}$, respectively. Sinusoidal current ($I = 20$ nA at 1 kHz) source S and potential recording electrode E are placed in the same domain (A) and in different domains (D). Distance d_{SE} is the length of line segment $|SE|$, and h_{S}, h_{E} are distance from S, E to boundary Ψ, respectively. Relative error distributions of potential magnitude and phase when E in Ω_1 with $d_{\mathrm{SE}} = 10$ mm (B, C) and E in Ω_2 with $d_{\mathrm{SE}} = 15$ mm (E, F) changing the conductivity $\sigma_2 = [0.01 \cdot \sigma_1, 100 \cdot \sigma_1]$ and relative permittivity $\varepsilon_{\mathrm{r2}} = [0.01 \cdot \varepsilon_{\mathrm{r1}}, 100 \cdot \varepsilon_{\mathrm{r1}}]$. Additional simulation parameters: $h_{\mathrm{S}} = h_{\mathrm{E}} = 5$ mm, $\sigma_1 = 0.431$ S/m, $\varepsilon_1 = 8.67 \times 10^5$ (dimensionless).

3.1 Simulation configuration

A surface Ψ divide full space into two domain $\Omega_{\{1,2\}}$ with conductivity $\sigma_{\{1,2\}}$ and relative permittivity $\varepsilon_{\{\mathrm{r1,r2}\}}$, respectively. The electrical property in Ω_1 is that of isotropic muscle, i.e., $\sigma_1 = 4.31 \times 10^{-1}$ S/m, $\varepsilon_{\mathrm{r1}} = 8.67 \times 10^5$ (dimensionless), while the electrical property in Ω_2 changes as $\sigma_2 = [0.01 \cdot \sigma_1, 100 \cdot \sigma_1]$, $\varepsilon_2 = [0.01 \cdot \varepsilon_1, 100 \cdot \varepsilon_1]$. A point-like source S located in Ω_1 generating sinusoidal current (I=20 nA at 1 kHz). An electrode E records the electrical potential U. To evaluate the accuracy, we define the magnitude error $e_{\mathrm{mag}} := \left(|U_{\mathrm{Theory}}| - |U_{\mathrm{FEM}}|\right)/|U_{\mathrm{FEM}}|$ and phase error $e_{\mathrm{phase}} := \left(\mathrm{Arg}\left\{U_{\mathrm{Theory}}\right\} - \mathrm{Arg}\left\{U_{\mathrm{FEM}}\right\}\right)/\mathrm{Arg}\left\{U_{\mathrm{FEM}}\right\}$ of electrical potential, where $\mathrm{Arg}\{\cdot\}$ is the argument of a complex value.

In case study 1, the potential recording electrode E can be placed in domain Ω_1 (see Figure C1 A) and in Ω_2 (see Figure C1 D). Geometrical parameters are set as constants: distance $d_{\mathrm{SE}} = 10$ mm is the length of line segment $|SE|$, and $h_{\mathrm{S}} = 5$ mm, $h_{\mathrm{E}} = 5$ mm are distance from S, E to planar boundary Ψ, respectively.

In case study 2, boundary Ψ is a spherical surface with radius $b = 5$ mm, and length $R_{\mathrm{S}} = 10$ mm, R_{E} are distance from S, E to spherical center point C. Electrode E can also be placed in domain Ω_1 with $R_{\mathrm{E}} = 8$ mm (see Figure B2 A) and in Ω_2 with $R_{\mathrm{E}} = 3$ mm (see Figure B2 D). Angle $\theta_{\mathrm{C}} = 90^{\circ}$ is the angle between of line segment $|EC|$ and $|SC|$.

3.2. Accuracy

Figure C1 and B2 plot the accuracy of the 1st-order electrical potential predictions compared to FEM simulation in case study 1 and 2, respectively. The conductivity and relative permittivity properties in domain Ω_2 change from 0.01 to 100 times to that in Ω_1 while keeping the geometrical parameters constants. The relative error of magnitude and phase are shown when electrode E located in domain Ω_1 (Figure C1 B and C in case study 1, Figure B2 B and C in case study 2) and in Ω_2 (Figure C1 E and F in case study 1, Figure B2 E and F in case study 2). The relative errors for magnitude and phase are $\leq 0.14\%$, $\leq 0.09\%$ in case study 1, and $\leq 0.8\%$, $\leq 7\%$ in case study 2, respectively. Of note, when electrical property in domain Ω_2 is set as fat (i.e., $\sigma_2/\sigma_1 = 0.052$ and $\varepsilon_2/\varepsilon_1 = 0.028$), the relative errors of magnitude and phase of electrical potential are both $\leq 0.5\%$.